

<https://doi.org/10.1038/s44310-024-00030-9>

Advances in resonator-based Kerr frequency combs with high conversion efficiencies

Xucheng Zhang^{1,2}, Chunxue Wang^{1,2}, Zhibo Cheng^{1,2}, Congyu Hu^{1,2}, Xingchen Ji^{1,2}✉ & Yikai Su²

Recent developments in resonator-based Kerr frequency combs promise excellent applications in a wide range of fields such as biosensing, spectroscopy, optical communications, light detection and ranging (LiDAR), frequency synthesis, astronomical detection, and quantum optics. A key figure of merit (FOM) for Kerr frequency combs is the pump-to-comb conversion efficiency, which is critical for applications requiring sufficient comb power and low power consumption. In this review, we first discuss the limited conversion efficiency of dissipative Kerr soliton in an anomalous dispersion microresonator based on its underlying physical characteristics. And then, we summarize the recent advances in Kerr frequency combs with high conversion efficiencies in both anomalous and normal dispersion regimes. We classify them according to various soliton states, excitation methods as well as novel material platforms. The final section of the paper presents an overview of current progress and glances at potential directions for future research.

Benefitting from advanced micro/nanofabrication technologies, Kerr frequency comb generation based on ultra-high-quality (Q) microresonators is a technique with the potential to revolutionize a variety of applications such as high-speed data transmission^{1–5}, LiDAR^{6–8}, spectroscopy^{9–12}, optical clocks^{13–16}, microwave photonics^{17–20}, machine learning^{21,22}, astronomical detection^{23,24}, and quantum optics^{25–28}. Over the past decade, significant progresses have been made towards integrated microresonator combs (also called “microcombs”) by using continuous-wave (CW) lasers—in two different group-velocity dispersion (GVD) regimes. For platforms displaying anomalous GVD, dissipative Kerr soliton (DKS) microcombs are generated through a double balance between parametric gain and optical losses, Kerr nonlinearity and dispersion²⁹. These self-confined waves exhibit a hyperbolic-secant squared (sech^2) profile in both the time and frequency domains, and illustrate remarkable coherence³⁰. Physically, DKS can be spontaneously organized when the driven CW laser, with an appropriate power, sweeps across a resonance of the microresonator from the blue to red detuning regime. In this process, the states of microcombs experience a continuous evolution from the primary combs to modulation instability (MI) combs, and (breathing) multi-soliton combs³⁰. When the multi-soliton state is generated from the chaotic MI state, the intracavity power drops dramatically and results in pump frequency shifting out of the cavity resonance through thermo-optical effect. Moreover, the randomness of the number of solitons further complicates this process. To overcome the strong

thermal-optical effect, one solution is using microresonators with a low thermal-optic coefficient, such as magnesium fluoride (MgF_2)^{30–34}. Another solution is realizing the intracavity thermal equilibrium, and various schemes have been implemented, such as power-kicking^{35–37}, thermal tuning^{38–41}, auxiliary-laser-assistance^{42–45}, phase modulation^{46,47}, photo-refractive effect^{48,49}, pulse pumping^{50–54}, and self-injecting-locking^{55–61}. Accompanying the exploration of enabling robust DKS access, rich types of DKS states have been discovered in anomalous GVD regime, such as breathers^{62–65}, Stokes soliton^{66,67}, soliton crystals^{49,68–70}, soliton molecules⁷¹, and laser cavity soliton^{72–74}. Different from the Kerr soliton frequency combs with various derivatives generated in the anomalous GVD regime, dark soliton (or dark pulse) is deemed as the exclusive mode-locked localized reduction structure in the normal GVD regime. Dark soliton generally manifested as intensity dips embedded in a high-intensity constant background with a complex temporal structure and a spectrum with a flat-topped envelope in the frequency domain^{39,40,65,75,76}. Compared with the bright solitons and soliton frequency combs generated in microresonators with anomalous dispersion, dark solitons are less sensitive to the system perturbations and have higher power conversion efficiency. These unique advantages have facilitated research on dark solitons and attracted increasing interest in many practical areas^{39,76–78}. All of the above achievements suggest that microresonator-based Kerr frequency combs can provide an ideal testbed for nonlinear physics and allow for the realization of a

¹John Hopcroft Center for Computer Science, School of Electronic Information and Electrical Engineering, Shanghai Jiao Tong University, Shanghai 200240, China.

²State Key Laboratory of Advanced Optical Communication Systems and Networks, Department of Electronic Engineering, Shanghai Jiao Tong University, Shanghai 200240, China. ✉e-mail: xingchenji@sjtu.edu.cn

portable integrated photonic device for use in out-of-the-laboratory applications.

Despite the discovery of rich physical phenomena—including breathers, Stokes solitons, soliton crystals, soliton molecules, laser cavity solitons, and dark solitons—relevant to DKS, and deeper insights into the dynamics of this new category of laser sources have been revealed, expanding the potential applications for comb-based integrated photonics, the quality of the generated microcombs, especially the power conversion efficiency limits its practical application scenario. Taking frequency combs as the carriers in communications as an example, the key parameter is the comb-line power, which should be greater than 1 mW as the data channel for modulation and detection⁷⁹. A low pump-to-comb conversion efficiency would require high-power sources and complex servo systems (e.g., thermal management), which greatly offset the advantages of low power consumption and portability of integrated photonics. However, extensive theoretical and experimental works have demonstrated the efficiency of single-soliton Kerr microcombs for a CW laser pump is limited to about 1%^{35,52,80–83}. The pump power required for holding the soliton in the anomalous dispersion regime is relatively higher compared to the maintained soliton power, and a majority of pump power is transmitted directly at a through port without coupling into the microresonator in order to satisfy the detuning state for obtaining the soliton³⁰. Fortunately, the demonstration of dark soliton alleviated the difficulty of boosting the pump-to-comb power conversion efficiency⁷⁷. Besides, with the development of fabrication process and improved dispersion/perturbation engineering, several approaches have been proposed to increase the efficiency in a Kerr resonator, such as synchronously pulsed pumping^{50,52}, steadily accessed multi-soliton based on self-injection locking⁸⁴, synthesized soliton crystals⁸⁵, laser cavity soliton, and assisted auxiliary microresonator^{40,86}. Representatively, a dark soliton microcombs generated in a Si₃N₄ resonator with an on-chip conversion efficiency above 20% has been utilized in a coherent communications scheme, realizing a bit-error rate (BER) below 10^{−15} with an aggregate data rate of 4.4 Tbps⁷⁸. Dual three-soliton-state combs with slightly different line spacing and a conversion efficiency of up to 40% have been demonstrated by using the self-injection locking method and integrated as a coherent dual-comb spectrometer⁸⁴. Nevertheless, significant improvement of conversion efficiency remains challenging, and there is no decisive approach to produce a high-efficiency Kerr frequency combs while combining other advantages (such as wide bandwidth, high comb-line power, low noise, narrow linewidth, etc.) that can offer a strong promise as a universal laser source for a variety of applications.

In this review, we provide an overview of the recent developments in resonator-based Kerr frequency combs technology towards boosting the pump-to-comb power conversion efficiency. The paper is organized as follows: Firstly, we will start with the demonstration and analysis of the efficiency of single-soliton microcombs. Secondly, we will focus on the emerging schemes for improving the conversion efficiency of Kerr frequency combs in both anomalous and normal GVD regimes, including synchronously pulsed pumping, multi-soliton microcombs, soliton crystals, dark solitons, laser cavity solitons, and assisted auxiliary microresonators. Finally, a brief summary and outlook on the underlying challenges for this field are presented.

Single-soliton microcombs in anomalous GVD regime

The demonstration of mode-locking DKS in a high-Q MgF₂ microresonator triggered a boom in the study of soliton microcombs and became a paradigm for the generation of temporal solitons and microcombs³⁰. The adopted experimental setup is shown in Fig. 1a, where a tunable narrow-linewidth laser is used as the pump and coupled into the MgF₂ crystal whispering gallery microresonator with anomalous dispersion. By changing the laser frequency with an appropriate scanning speed to sweep over one cavity resonance from blue detuning to red detuning regime, DKSs are obtained and measured at the through port. In this work, several key features of temporal solitons and soliton microcombs have been found and demonstrated repeatedly in subsequent studies: (1) the transmission power

trace presents a triangular resonance shape with increasing intensity oscillations before the pump reaches the zero-detuning point, as shown in Fig. 1b. This process can be divided into three states to depict the successive evolution of the intracavity optical field in the blue detuning regime, which includes the primary comb (I), subcomb (II), and MI comb (III). The corresponding optical spectra are shown in Fig. 1c. (2) The triangular resonance shape deviates into discrete steps when the pump scans in the red detuning regime, indicating the formation of dispersive solitons and a decrease in the number of solitons. (3) The spectral shape of the comb spectrum exhibits a sech² functional form of a single-soliton state and a modulated envelope for multi-soliton states. In the time domain, the output consists of ultrashort pulses with a period equal to the round-trip time or a subharmonic thereof (Fig. 1e). (4) The DKSs states are fully coherent, as evidenced by the excellent low-noise characteristics of the corresponding beat notes (insets of Fig. 1d), and this coherence is reflected in the consistency between the sech²-shaped power profile and spectral envelope for the single-soliton state (Fig. 1f).

Taking advantage of the smooth spectral envelope and fixed temporal spacing, single-soliton microcombs are favored for practical applications. However, as aforementioned, the DKSs can be formed through MI by tuning the laser from the blue side of the resonance towards the red in a resonator with bistability, and it can only be maintained with the laser effectively red-detuned. The high laser detuning results in most of the pump power being reflected, thus not coupled into the micro-resonator and involved in the formation of DKSs. This imposes a fundamental limitation on the conversion efficiency, especially for the single-soliton state. It suffers from a sudden drop in microcombs power and exhibits a staircase step in transmission trace (Fig. 1b) when transitioning from multi-soliton states. In addition, the conversion efficiency is further limited due to the saturation of the parametric gain determined by the characteristics of the microresonators^{80,87–89}. In the case of single DKS microcombs generated in anomalous GVD regime, the comb lines carry less than 1% of the input pump power. The low conversion efficiency significantly undermines the practical appeal of single-soliton microcombs. Moreover, with the rapid development of modern micro/nanofabrication technologies, the power consumption of soliton microcombs decreases, leading to a lower power of comb lines due to the relatively fixed parameter space for generating DKSs. The low pump-to-comb power conversion efficiency of conventional single-soliton microcombs has not been bolstered by the development trend of low-power consumption and advanced micro-nanophotonics, and even has gradually fallen out of line with the development needs of practical applications.

While the conversion efficiency of single-soliton microcombs is primarily determined by the inherent properties of DKS formed in microresonators, several parameters can affect the exact value of conversion efficiency. Firstly, the power coupling coefficient between the microresonator and bus waveguide plays a crucial role. Figure 2a illustrates the dependence of nonlinear conversion efficiency and intracavity pulse energy on the power coupling coefficient⁸⁰, revealing a square root dependence of the conversion efficiency on the power coupling coefficient. Obviously, a larger power coupling coefficient allows more pump power to be coupled into the resonator for conversion into a microcomb, resulting in a higher microcomb power being coupled out. Consequently, the increase in conversion efficiency is accompanied by a decrease in intracavity pulse energy. In practice, increasing the power coupling coefficient is a straightforward method to extract intracavity power from high-Q microresonators. Therefore, there is considerable research on microresonators with anomalous and normal dispersions, operating in highly over-coupled regime to generate microcombs with high pump-to-comb power conversion efficiency^{52,77,90–92}. Secondly, a higher (anomalous) dispersion coefficient is beneficial to improve conversion efficiency. As shown in Fig. 2b, a microresonator waveguide with a higher dispersion coefficient (slot waveguide 2, $\beta_2 = -87$ ps²/km) can generate a microcomb with a narrower bandwidth, corresponding to a wider pulse and theoretically resulting in a higher conversion efficiency⁸⁰. Thirdly, the input (or pump) power exhibits a

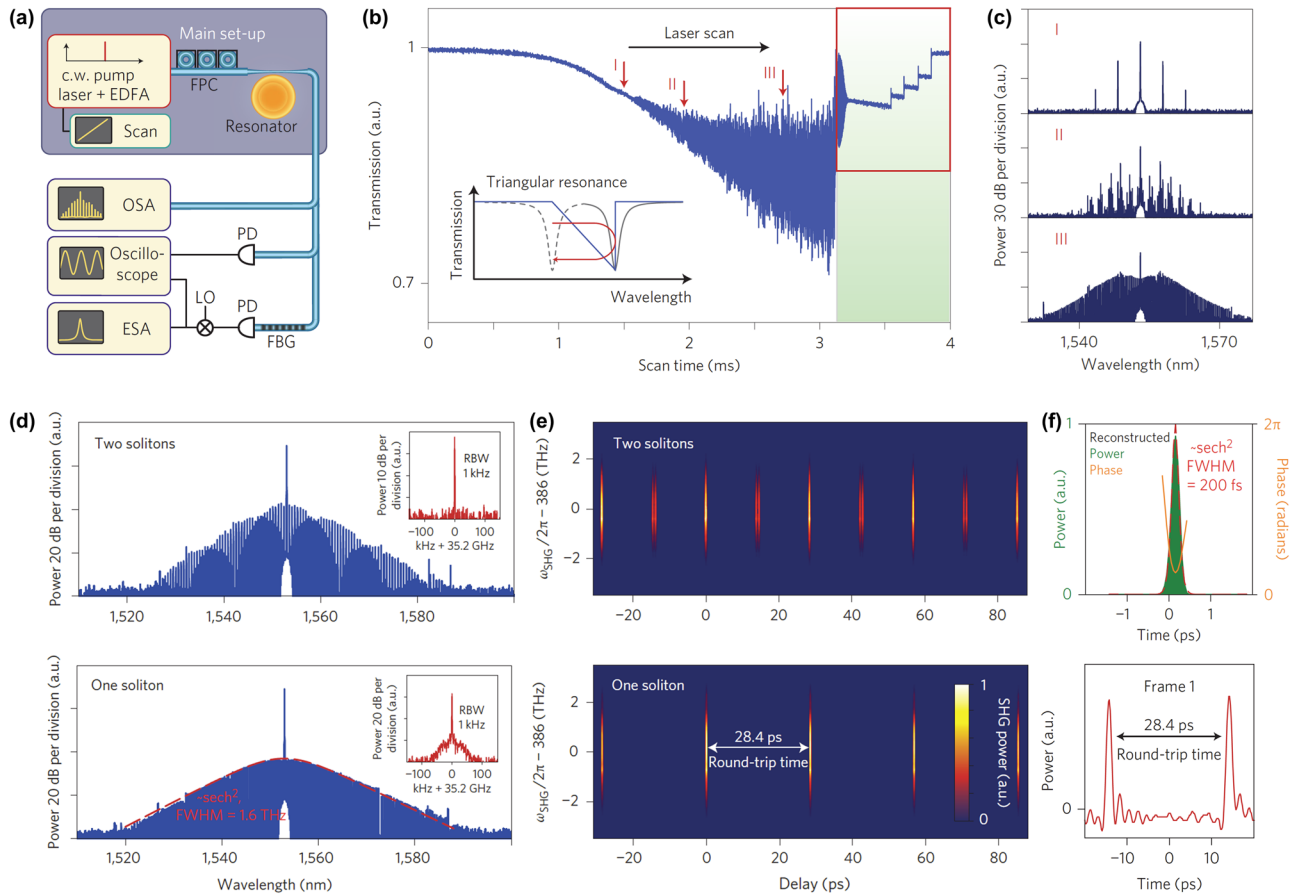


Fig. 1 | Experimental demonstration of single-soliton Kerr combs in a MgF₂ microresonator using the frequency-scanning method. **a** Experimental setup for DKS generation. **b** Transmission observed when scanning the CW laser over a resonance from the blue detuning to red detuning regime (green shading). Solitons are generated in the red detuning regime and then annihilated to form discrete steps in the further red detuning regime. The inset shows the Lorentzian resonance shape of the cold microresonator (dashed line) and the triangular resonance shape under the combined Kerr and thermal effects of the strongly driven microresonator (solid line). **c** Optical spectra of three different states (marked in **b**) for the CW laser scanning in the blue regime. **d** Optical spectra of Kerr combs with 2 and 1 solitons.

The insets show the radio frequency beatnote. **e** Measured frequency-resolved optical gating (FROG) traces of the two-soliton and single-soliton pulses. **f** The reconstruction of power profile (the red dashed line with a sech² shape) and phase (the yellow solid line) of pulse (top panel), and sampled optical power of the output over a duration of 40 ps (bottom panel) of the single-soliton pulses. OSA optical spectrum analyzer, ESA electrical spectrum analyzer, PD photodetector, LO local oscillator, FPC fiber polarization controller, EDFA erbium doped fiber amplifier. Images are adapted with permission from ref. 30. Copyright 2014 Springer Nature Limited.

relationship between the reciprocal of square root and the conversion efficiency, as illustrated in Fig. 2b, $g^{80,81}$. As the pump power increases, the conversion efficiency converges to a constant value due to the parametric gain saturation effect. Fourthly, in the parameter space where DKS exists, the conversion efficiency increases with larger pump detuning (i.e., positive-slope soliton stairs as shown in Fig. 2c)^{30,80}. The underlying physical mechanism behind that lies in the increase in soliton peak power being more prominent than the decrease in soliton pulse width (caused by the larger detuning) to maintain soliton self-thermal-locking. In addition, since the pulses share almost the same shapes and coherence in single-soliton and multi-soliton states, the conversion efficiency is proportional to the reduction of the number of pulses in the further red-detuned regime.

Starting from an approximate analytical expression derived from the single soliton solution for the Lugiato–Lefever equation (LLE)^{93–95}, which serves as the universal and successful model for depicting microcombs dynamics in the Kerr microresonator, the conversion efficiency can be expressed as^{80,81}

$$\eta = \frac{2\pi\theta}{\theta + \alpha_i L} \sqrt{\frac{|\beta_2|}{\gamma P_{in}}} \cdot \text{FSR}, \quad (1)$$

where η is the conversion efficiency defined as the ratio of the total output comb power excluding the pump mode to the input pump power, θ is the power coupling coefficient, α_i is the propagation loss coefficient, L is the resonator length, β_2 and γ are the dispersion and Kerr coefficients, respectively, P_{in} is the input pump power, and FSR is the cavity free spectral range. It is noted that the Eq. (1) is derived from an assumption that the soliton locates at the theoretical maximum detuning of $\Delta_{\max} = \delta_{0, \max}/\alpha = \pi^2 \gamma L \theta P_{in}/(8\alpha^3)$, with $\alpha = (\theta + \alpha_i L)/2$, and δ_0 is the phase detuning of the nearest resonance with respect to the pump frequency. Equation (1) provides straightforward insight into how the conversion efficiency scales with various parameters. Therefore, in addition to the parameters discussed above, factors such as the Kerr coefficient, propagation loss, and FSR of the resonator will also impact the conversion efficiency. Notably, Jang et al. further revealed three distinct scaling regimes of conversion efficiency with the FSR, contingent upon the coupling state of microresonators⁸¹. Specifically, the conversion efficiency displays square-root, square, and linear dependence on FSR for near critical coupling, highly under-coupled, and highly over coupled, respectively, as shown in Fig. 2d–f) It is obvious that improving the conversion efficiency of single-soliton microcombs is a complex problem involving multiple parameters, and the microcomb need to synthesize the delicate balance between these parameters, making it difficult to define a fundamental limitation on the conversion efficiency of single-soliton

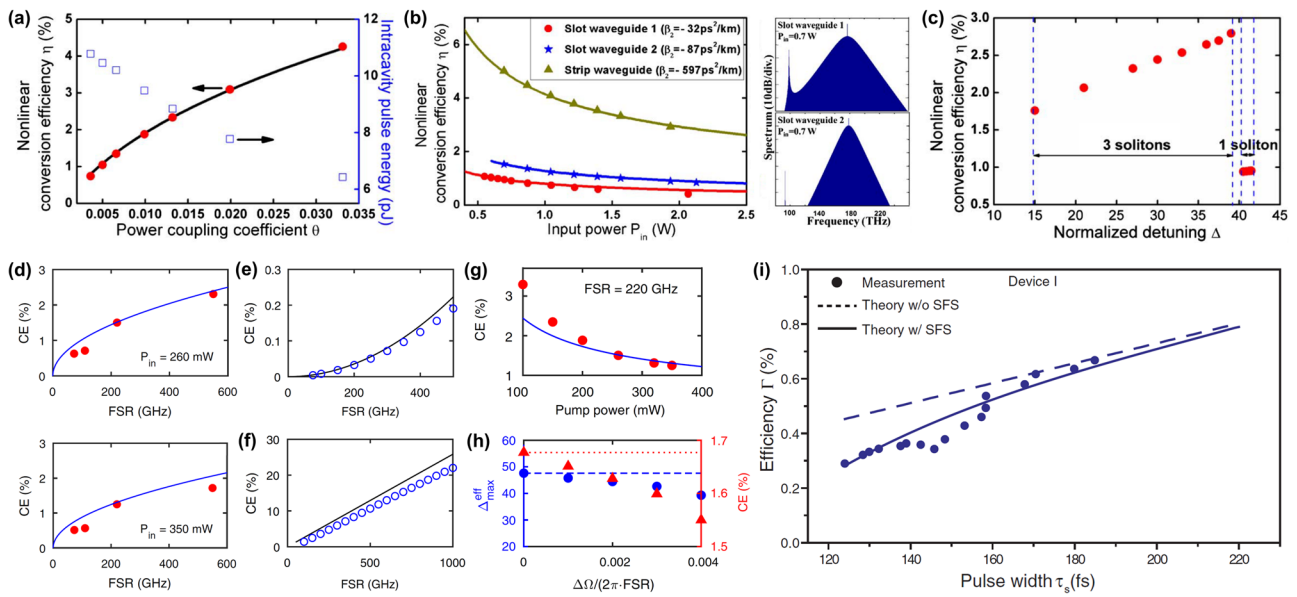


Fig. 2 | Conversion efficiency of single-soliton microcombs. **a** Conversion efficiency and intracavity pulse energy versus power coupling coefficient⁸⁰. **b** Conversion efficiency versus the input power with different dispersion coefficients. An example of the intracavity single-soliton microcombs corresponding to different slot waveguide is shown in the right panel⁸⁰. **c** The dependence of conversion efficiency on the pump frequency detuning⁸⁰. **d** Scaling of the conversion efficiency with the cavity FSR for the pump powers of 260 mW and 350 mW for critical-coupled regime. Red circles and the blue curves represent the experimental results and theoretical predictions, respectively⁸¹. FSR scaling of the conversion efficiency between theory (black curve) and simulation (blue circles) for **(e)** highly under-coupled and **(f)** highly over-coupled regimes⁸¹. **g** Conversion efficiency versus the

pump power with an FSR of 220 GHz. Red circles and the blue curves represent the experimental results and theoretical predictions, respectively⁸¹. **h** Effects of a mode crossing on the maximum effective detuning accessible (blue circles) and corresponding conversion efficiency (red triangles). Dashed blue line and dotted red line show the maximum effective detuning and conversion efficiency, respectively, in the absence of a mode crossing⁸¹. **i** Measured efficiency versus soliton pulse width is plotted (blue points) for two devices and compared with theory. A theoretical comparison with Raman (solid blue lines) and without Raman (dashed blue lines) is presented⁸³. CE conversion efficiency, FSR free spectral range, SFS self-frequency shift. Images are adapted with permission from refs. 80,81,83. Copyright 2014,2016,2021 Optical Publishing Group.

microcombs. Recently, there are some studies on surpassing the conversion efficiency of soliton microcombs by optimizing multiple parameters of resonators^{96–98}, which revealed, in numerical or experimental ways, that the conversion efficiency can be effectively improved by amplifying multiple favorable parameters (e.g., dispersion coefficient, power coupling coefficient, and FSR) and/or minishing the unfavorable parameters (e.g., loss and Kerr coefficient).

In addition to the fundamental properties of microresonators, there are some nonlinear effects that are detrimental to the conversion efficiency. Notably, Fig. 2h, i presents the effects of mode crossing and self-frequency shift (SFS) on conversion efficiency^{81,83}. Comparing the maximum conversion efficiency in the absence of a mode crossing (dotted red line in Fig. 2h), the existence of a mode crossing reduces the detuning range of soliton and the maximum conversion efficiency that can be achieved (blue circles and red triangles in Fig. 2h). The SFS effect caused by the Raman nonlinearity would shift the energy of the soliton spectrum from the blue side to the red. Such redistribution of soliton energy increases the minimum pumping power for generating soliton and results in the decrease of energy conversion efficiency.

Schemes for generating high-efficiency Kerr microcombs

The low conversion efficiency of soliton microcombs can be attributed to the small temporal overlap between the CW pump laser and the ultrashort soliton pulse generated in anomalous GVD regime. In contrast, the dark pulse formed in normal GVD regime can be inversely regarded as a wide bright soliton that has a high duty cycle and thus a high conversion efficiency. The optimization of single-soliton microcombs parameters to improve conversion efficiency involves increasing dispersion coefficient, increasing FSR of resonator, and achieving over-coupling state, is intended to increase the temporal overlap between soliton pulse and the CW

background. Combining the various nonlinear dynamics of soliton, the extraordinary soliton states of multi-solitons, soliton crystals, dark pulses, and laser cavity solitons inherently present a larger temporal overlap with the CW background (even background-free for laser cavity solitons) and hence a larger pump-to-comb power conversion efficiency. In particular, it is an effective method to improve the conversion efficiency by replacing the CW laser with a pulse laser that has a focus intensity profile. Additionally, feedback architectures can also be utilized to recycle the CW pump power, further contributing to improve conversion efficiency. Based on the advantages of high coherence and low noise, soliton microcombs with high conversion efficiency are desired for many practical applications, and has aroused extensive research interest. In this section, we will focus on the schemes for generating microcombs in Kerr resonators with high conversion efficiency.

Pulse pumped soliton microcombs

Distinct from the conventional narrow-linewidth CW lasers, temporally structured light sources can also be used as a pump for soliton microcombs generation. The principles for CW-driven and pulse-driven schemes are presented in Fig. 3a, b, respectively⁵⁰. In a Kerr microresonator, the CW pump field builds up through cavity enhancement and leads to parametric gain for other cavity modes. Once the gain exceeds the cavity loss, parametric oscillation occurs and Kerr frequency comb generated based on a nonlinear optical process of four-wave mixing (FWM). Under suitable conditions of the balance between Kerr nonlinearity and dispersion along with the balance between parametric gain and loss, the stimulated cavity modes would be phase-locked, forming soliton pulse within the CW background in the time domain. Similarly, the soliton driven by optical pulse formed in a nonlinear optical microresonator undergoes nearly identical nonlinear evolution. In the first pulse-driven soliton microcombs generation experiment, an electro-optic modulation (EOM) picosecond

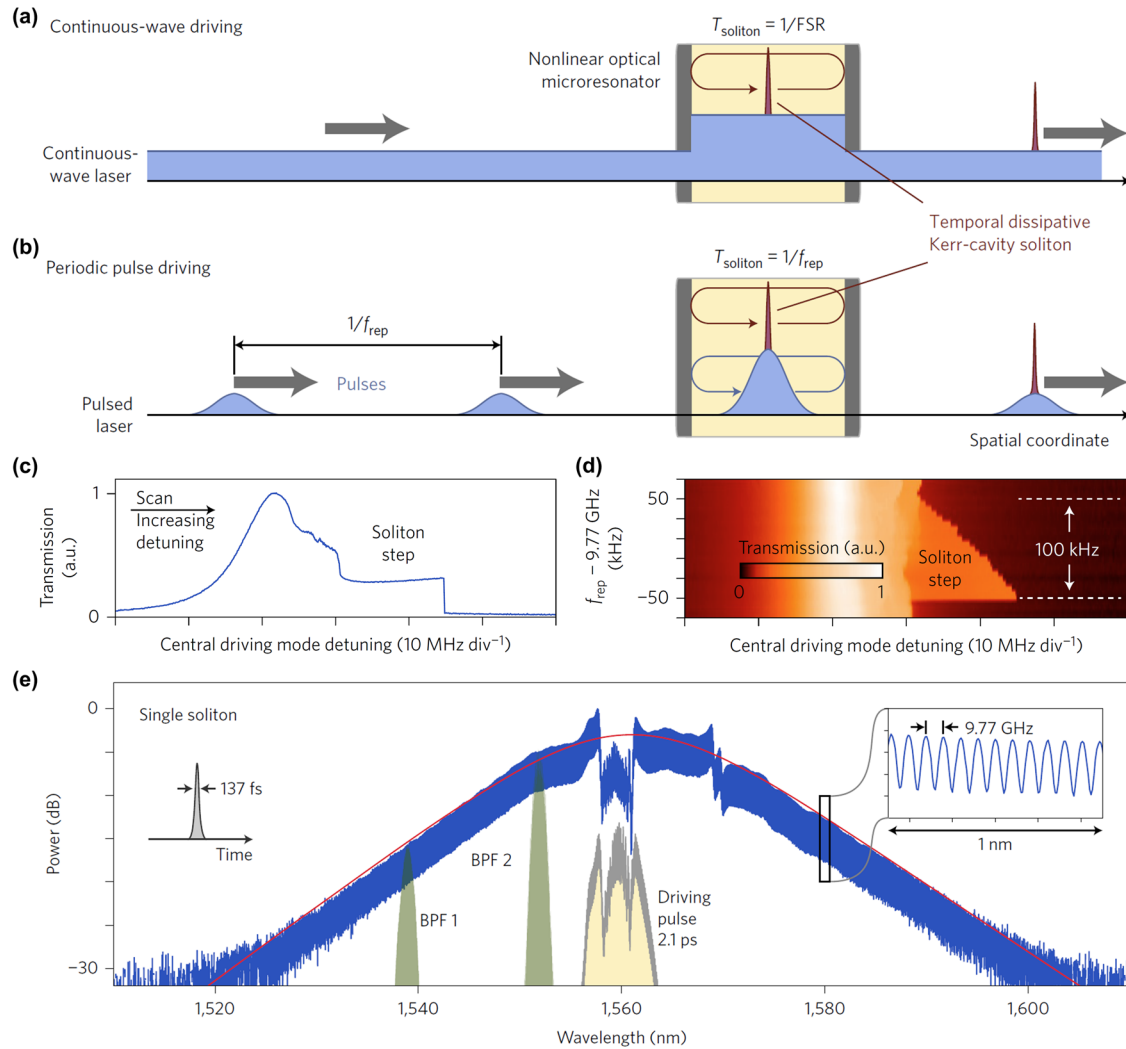


Fig. 3 | Soliton microcombs driven by optical pulses. **a** Principle of continuous-wave-driven soliton frequency combs. A DKS propagates with a roundtrip time defined by the resonator’s inverse FSR while being supported by the resonant enhanced CW background. **b** Principle of pulse-driven soliton frequency combs. Stable solitons form atop the optical pulse with a repetition rate that coincides with the resonator’s FSR. **c** Resonator transmission trace obtained when the central driving mode scans across a resonance for an optimized pulse repetition rate. **d** Contour plot of the transmission showing soliton step existing over a wide

(100 kHz) interval of repetition rate. **e** Optical spectrum of a single soliton driven by a pulse with a duration of 2.1 ps (which corresponds to the yellow spectrum in the frequency domain). The sech^2 -envelope fit (red) corresponds to a soliton pulse duration of 137 fs (the inset on the left). The inset on the right shows a magnified view of the spectrum in a 1 nm range. The green spectra show the transmission spectra of the bandpass filters (BPF 1 and 2) used for beatnote detection. Images are adapted with permission from ref. 50. Copyright 2017 Springer Nature Limited.

pulse generator served as the pump source to drive a monolithic fiber Fabry–Perot (FP) resonator with an FSR of ~ 9.8 GHz⁵⁰. As the repetition rate of the picosecond pulse, controlled by the radio frequency (RF) generator, matches the FSR of the resonator, the stable femtosecond soliton would be generated ‘on top’ of the resonantly enhanced driving pulse, as shown in Fig. 3b. As the central driving mode scans across a resonance from the blue-detuning to red-detuning regimes, the resonator transmission shows characteristic soliton step features, as shown in Fig. 3c. The generated soliton microcomb is presented in Fig. 3e, with the spectrum corresponding to a single pulse of 137 fs duration, exhibiting a sech^2 -shape envelope. The soliton step appears for a wide spanning interval (100 kHz) of driving pulse repetition rate f_{rep} (Fig. 3d), suggesting the soliton obtained in a pulsed driving system is robust for resisting the random fluctuations of value of f_{rep} . In contrast to CW-driven systems, the pulse laser offers a significantly higher peak power, alleviating constraints on the soliton microcombs generated in a high-Q microresonator with a small FSR and decreases the average driving laser power for generating solitons. Besides, the soliton can be robustly “trapped” at a specific position (not always sit atop the peak)

within the intracavity pump pulse, thus the microcomb’s repetition rate is locked to the driving pulse train and synchronized to the FSR of resonator while concomitantly suppressing its time jitter. Particularly, benefiting from the temporally focused structure of the driving pulse, there is a large overlap between the binding soliton and the driving pulse, leading to high power conversion efficiency. A 5% soliton conversion efficiency was measured in the first pulse-driven soliton microcombs experiment.

After the pulse-driven cavity soliton generation in fiber loop and FP resonator^{50,99}, the same scheme has also been transplanted to chip-scale microresonators^{51,52,54}. Since then, pulse-driven microcombs have been demonstrated with higher conversion efficiency. Anderson et al. used a high-Q silicon-nitride (SiN) microresonators with a designed low GVD and a strong third-order dispersion, generating a soliton microcombs with an electronically detectable repetition rate of 28 GHz, and measured a conversion efficiency of 8%¹⁰⁰. For the same device, a broadband soliton microcombs close to two-thirds of an octave formed with the aid of the strong dispersive wave emission, demonstrated an efficiency of 2.8% under a pulse driving with an

average energy of 6.4 pJ^{100} . The bandwidth of such broadband soliton microcomb is comparable to that of a supercontinuum, as noted by the authors. Li et al. analytically and experimentally investigated the influence of pulse-driven system parameters on the conversion efficiency of soliton microcombs, revealing unique soliton dynamics compared to CW driving and its limitations⁵². The experimental setup used is shown in Fig. 4a, with an EO comb (as shown in inset of Fig. 4b) utilized to generate pump pulses. The pulses had repetition rates synchronized to the FSR of the silica (SiO_2) microdisk resonator. Soliton generation was triggered when the center frequency of the pump pulse swept across the microcavity resonance from blue to red detuning regime. Examples of the soliton microcombs for the resonators with external Q factors (Q_{ex}) of 14 million and 37 million are illustrated in Fig. 4b, in which a higher soliton output for the lower Q_{ex} is consistent with the trend of power coupling coefficient imposed on conversion efficiency. Figure 4c presents the measured soliton conversion efficiency versus Q_{ex} for different durations of pulses, with the pulse duration adjusted by controlling the number of EO comb lines. The soliton efficiency increases as the duration of pumping pulse decreases. Theoretically, this trend is valid until the pump pulse width is smaller than the width of the formed soliton pulse. Remarkably, single-soliton operation with a steady-state conversion efficiency up to 34% is attained using 2 ps pump pulses, while a transient efficiency up to 54% is measured using 1 ps pump pulses under frequency-scanning conditions. These record high efficiencies demonstrate the conversion efficiency of soliton microcombs can be significantly boosted by optimizing the pulse-driven system.

Besides the pulse-driven system working in anomalous dispersion, recently, the pulse driven methods were demonstrated for generating dark pulses in normal-dispersion resonators. The first normal-dispersion soliton microcombs driven by pulse was formed in a weakly normal SiN microresonator in the near-zero-dispersion regime¹⁰¹, in which the complex interplay between switching waves (SWs) and dispersive solitons was fully investigated and achieved a near-octave broadband microcomb. At the same time, the soliton dynamics in a strong normal-dispersion resonator was studied by ref. 102. Both studies demonstrated that pulsed driving enables the spontaneous generation of isolated SWs, without requiring perturbations to the resonator's dispersion to induce MI. Following these works, the dynamics of normal-dispersion combs in fiber loop and FP resonators were studied^{53,103–105}, in which a conversion efficiency of 19% was measured in a FP resonator (with FSR $\sim 10.214 \text{ GHz}$) driven by a pulse with a duration of 1.9 ps^{104} , and a following conversion efficiency of 23.4% was achieved by the same research group in a FP resonator with an FSR of 1.8393 GHz^{105} .

Researches have been done to explore combination of pulsed driving scheme with other effects. Simply, taking advantage of the bonding effect between pump pulses and solitons (or soliton self-synchronization effect), the microcombs with tunable comb line spacing were achieved by applying a pulsed pump rate that is the rational harmonic of the resonator FSR^{101,106}. Physically, the dual-wavelength pumping schemes consisting of two laser beams very close in frequency are the roughest pulsed pumping sources⁸⁵, which were used to stimulate Brillouin lasers in fiber loops and driven internally to spontaneously generated soliton microcombs with low noise and high stability^{107,108}. Furthermore, the combination of self-injection locking and pulsed driving method enables the realization of fully integrated soliton microcomb sources⁵⁴, which were implemented to demonstrate a stable direct atomic spectroscopy with absolute optical-frequency fluctuations at the kilohertz level over a few seconds and $<1 \text{ MHz}$ day-to-day accuracy¹⁰. In addition, the pulsed driving scheme supports researches on other soliton physics, such as soliton tweezing¹⁰⁹, spontaneous symmetry breaking¹¹⁰, and Faraday instability¹¹¹. In summary, a superior soliton microcomb with greater performances (e.g., a higher conversion efficiency, a wider spectral bandwidth, a lower power consumption, and so on) is expectable in an optimized pulsed driving system combining other favorable effects.

Multi-soliton microcombs

Aforementioned, the microcombs in multi-soliton state have a larger energy that is scaled up proportionally with the number of solitons, which should be a strong candidate for improving the conversion efficiency considering its prevalence accompanying almost all single-soliton microcomb production^{30,31,35,42}. However, due to the inherently stochastic intracavity dynamics, the number of solitons generated in resonators is probabilistic in the usual approach in which detuning is swept to a predetermined value with input held constant. Figures 5a, b presents an example illustrating the overlapped power traces of one CW pump laser swept over a microresonator's resonance for 200 times using forward frequency-tuning method from blue to red detuning regime, which clearly shows the randomness of soliton number N . To achieve deterministic generation of single-soliton microcombs, a forward and backward frequency-tuning technique was introduced³¹. Briefly, this technique involves initially applying forward frequency tuning to stimulate multi-soliton state, and then the pump laser is swept backward adiabatically with a low scanning speed. During the operation of the latter, the soliton state switched successively by reducing the number of solitons one by one, as shown in the conceptual diagram in Fig. 5c. The experimental cavity dynamics of the forward and backward frequency-tuning method are shown in Fig. 5d, in which a regular staircase pattern is formed with the successive extinction of intracavity solitons. Incidentally, the nearly equal stair heights confirm the consistency between the pulse energies of multiple solitons. Figure 5e–g present the measured soliton microcombs in soliton states with $N = 1, 2, 3$, respectively, through the forward and backward tuning method. Although this method aims to deterministically obtain single soliton state, it involves continuously traversing the soliton state starting from the maximum number of solitons. Such characteristic makes it a technique for generating multi-soliton states containing a specific number of solitons. However, for a given dispersion coefficient, the number of solitons that can be generated has a maximum value, which is randomly determined during the forward tuning process (Fig. 5b). Therefore, it is not a robust approach to significantly improve the conversion efficiency based on the multi-soliton states with high N values.

Benefitting from the investigation on the self-injection locking effect, reproducible multi-soliton microcombs with high conversion efficiency were demonstrated on a hybrid integrated platform⁸⁴. The self-injection locking effect is a profound phenomenon in oscillatory circuits, extensively studied for decades in radio-physics, microwave electronics, and photonic integrated circuits to improve the spectral purity of the devices^{55,59,112–114}. Recently, this effect has been used in nonlinear photonics to facilitate the integration of microcombs. The principle of self-injection locking enabling the generation of soliton microcombs in a SiN microresonator is presented in Fig. 6a. In such setup, a single frequency laser launched by a free-running distributed feedback (DFB) diode is coupled into the resonator, and a portion of the laser radiation is resonantly backscattered (e.g., due to Rayleigh scattering here, or direct reflection in FP cavities) to the laser cavity. This process induces self-injection locking, effectively locking the laser emission frequency to the cavity mode of similar frequency¹¹⁵. The locked laser exhibits a dramatically reduced linewidth and noise, and further driving the nonlinear resonator to generate soliton microcombs. Since the back-reflection time is shorter than the thermal relaxation time, the laser frequency tracks the thermally shifted cavity resonance, effectively suppressing thermal instability and alleviating the requirement for delicate frequency manipulation to trigger solitons, which further enables a unique state of permitting soliton generation called “turnkey” operation through simply turning on the pump laser free from any additional auxiliary systems⁵⁷. The employed self-injection locking scheme enabled microcomb generation using high-performance semiconductor laser diodes instead of bulky narrow-linewidth lasers, thereby paving the way for the development of fully integrated chip-scale single microcomb sources. Using this method, Dmitriev et al. demonstrated a fully integrated, power-efficient dual-microcomb source operating in multi-soliton states⁸⁴. The merit of self-injection locking against thermal frequency drift broadens the soliton range (Fig. 6b) and enables turnkey operation. Remarkably, two types of

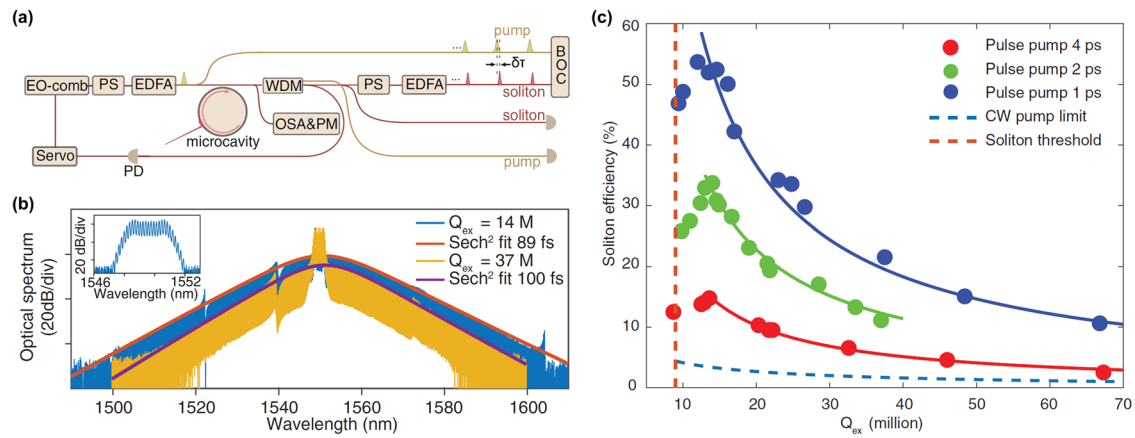


Fig. 4 | Pulse-driven soliton microcombs with high conversion efficiency. **a** Experimental setup. **b** Optical spectra of pulse-driven solitons generated in microdisks with $Q_{ex} = 14$ million (blue) and 37 million (yellow). The soliton output power is lower for higher Q_{ex} at the same pump power. Inset shows the electro-optical (EO) comb used to generate pump pulses. **c** Measured soliton conversion efficiency versus Q_{ex} for different durations of pulses. The solid curves are inverse

Q_{ex} fits of the measured efficiencies. The blue dashed line is the soliton efficiency under the CW pumping case. The red dashed line is the theoretical threshold Q_{ex} for soliton formation. WDM wavelength division multiplexer, PS pulse shaper, PM power meter, BOC balanced optical cross-correlator. Images are adapted with permission from ref. 52. Copyright 2022 Optica Publishing Group.

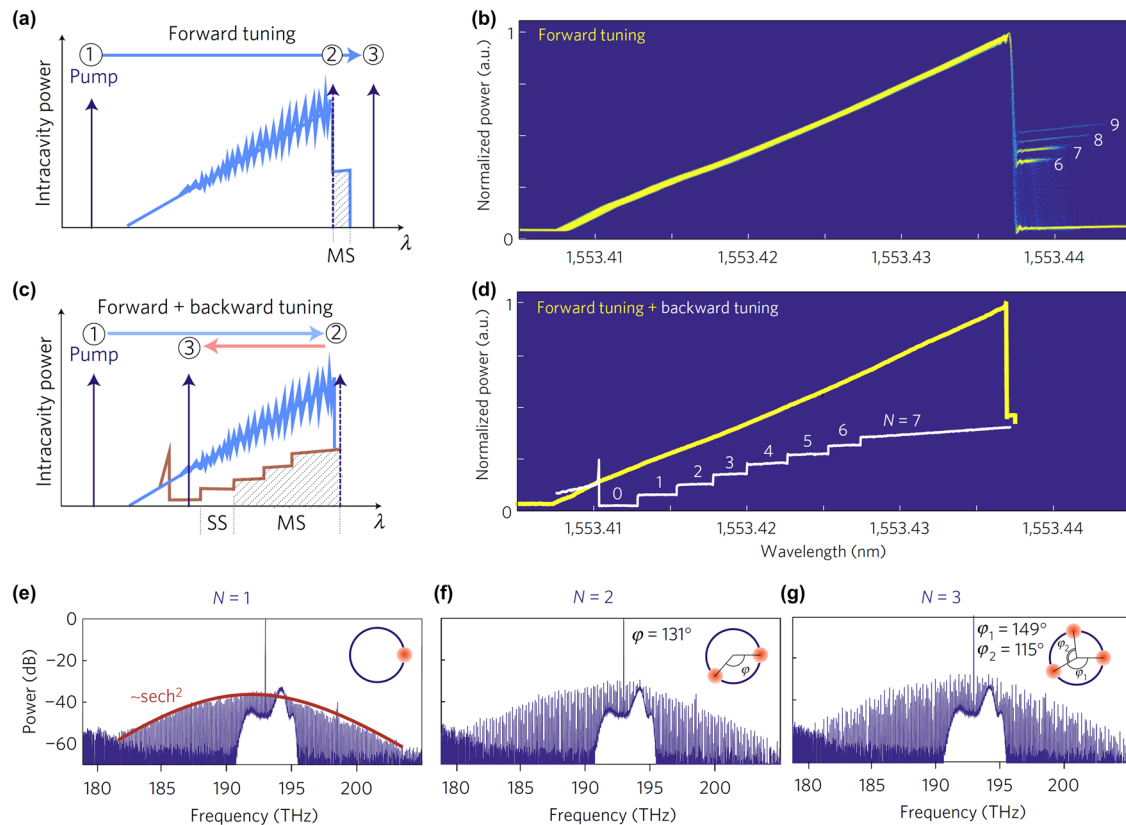


Fig. 5 | Forward and backward frequency-tuning methods. **a** Scheme of the forward tuning method for the soliton generation. The pump laser is tuned over the resonance from short to long wavelengths (forward tuning). Hatched region represents the range for multi-soliton (MS) states. **b** 200 overlaid experimental power traces of the output comb light in the pump forward tuning over the resonance, reveals the formation of a predominant multiple-soliton state with $N = 6$. **c** Scheme of the backward tuning method, where the forward tuning is first applied, and stopped in a multiple-soliton state, then the pump is tuned backward to access to

single-soliton (SS) state. **d** Experimental power trace in forward tuning (yellow curve) and the followed backward tuning (white curve) for soliton switch (from $N = 7$ to $N = 0$ successively) and deterministic single soliton generation. **e-g** Measured soliton microcombs in soliton states with $N = 1, 2, 3$, generated in a 100 GHz SiN microresonators during the backward tuning. The red solid curve shows the sech^2 fitting of the soliton spectrum envelope. Insets show the relative positions of the soliton inside the resonator. Images are adapted with permission from ref. 31. Copyright 2017 Springer Nature Limited.

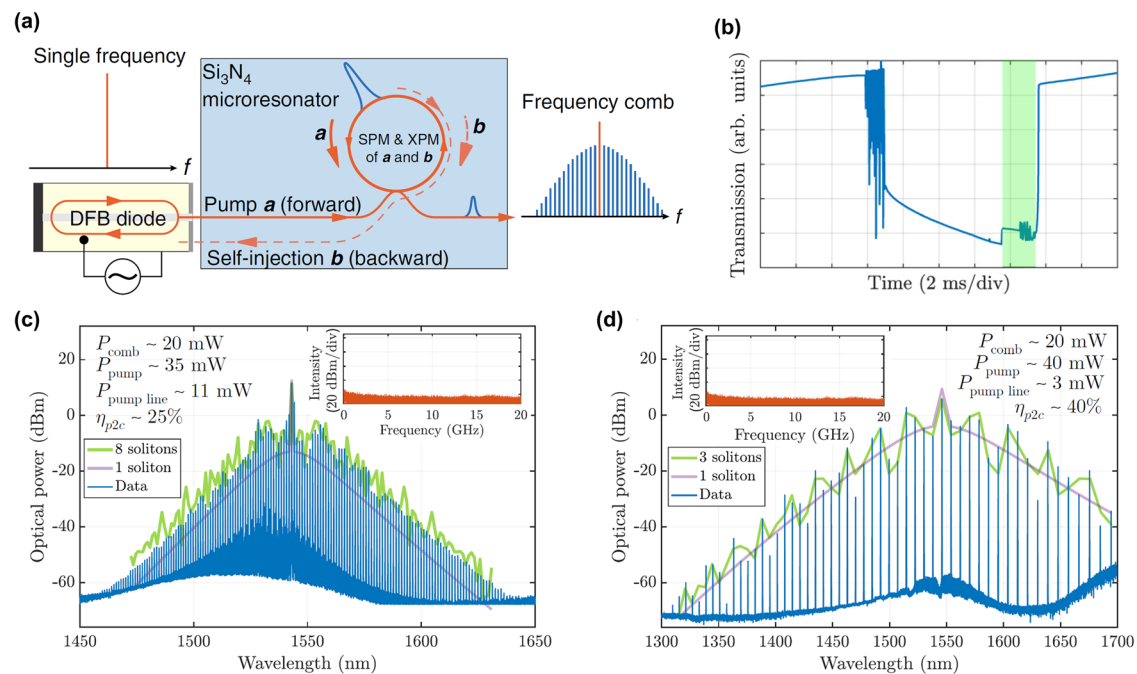


Fig. 6 | Multi-soliton microcombs generation based on self-injection locking effect. **a** Principle of self-injection locking. The distributed feedback (DFB) laser self-injection locks to a high-Q resonator via Rayleigh backscattering. Simultaneously, it pumps the nonlinear resonator to generate a soliton microcomb, wherein the nonlinear effects such as self-phase modulation (SPM) and cross-phase modulation (XPM) on self-injection locking are considered¹¹⁵. **b** Measured transmission trace for 35 mW pump power with self-injection locking effect. The green background

highlights the soliton existence⁸⁴. **c, d** Measured optical spectra (blue lines) of multi-soliton states for repetition rates of ~ 150 GHz (**c**) and ~ 1 THz (**d**). Green lines and purple lines represent the theoretical envelopes for multi-soliton state and single-soliton state, respectively. Insets show the RF spectra of the microcombs' intensity between 0 and 20 GHz⁸⁴. Images are adapted with permission from refs. 84,115. Copyright 2022 American Physical Society. Copyright 2021 Springer Nature Limited.

microcombs in eight-soliton (FSR ~ 150 GHz) and three-soliton states (FSR ~ 1 THz) with conversion efficiencies of up to 25 and 40%, respectively, were generated, as shown in Fig. 6c, d. It presents a record conversion efficiency for multi-soliton microcombs with broad spectra. Subsequently, the microcombs were further down-converted to the radio-frequency domain for applications in dual-microcomb spectroscopy.

Despite the realization of multi-soliton microcombs with high conversion efficiency enabled through self-injection locking, it is regrettable that the multi-soliton microcombs generally exhibit a structured spectrum determined by the relative positions of solitons in the microresonators, which are mostly random for the forward and backward tuning method and are ambiguous for self-injection locking^{90,116,117}. Overall, the challenge of accurately reproducing the same state and the significant intensity variations in the optical spectrum hinder the application of multi-soliton microcombs in fields that require smooth spectrum. This limitation also makes it less attractive in nonlinear physics research.

Soliton crystals microcombs

Among the various soliton phenomena in nonlinear resonator, soliton crystals are the most promising soliton-microcomb states with high conversion efficiency to be applied in practical applications. Soliton crystals were so-named due to their crystal-like patterns of ensembled copropagating solitons within Kerr resonators, which were self-organized and arranged with a regular sequence in distribution. Physically, the soliton crystals are a special class of multi-soliton states, and their generation is found to be related to the modulated background wave^{68,70}. Typically, this modulated wave is formed due to the presence of avoided mode crossings (AMXs), which occur as localized alterations of the microresonator dispersion resulting from interference between the pump mode and other transverse modes (as shown in Fig. 7b)⁷⁰. The modulated background serves as an optical lattice trap to “catch” the solitons at regular positions, leading to the ordering of DKS pulses in a crystal-like structure. Consistent with the

multi-soliton state, the power of microcombs in soliton crystals states linearly increased with the soliton number. A soliton crystal containing a sufficient number of packed solitons and filling the entire angular domain of the resonator exhibits an intracavity power similar to the MI state, it is presented by a typical soliton crystals step appearing at the peak of the transmission power trace following chaotic fluctuation stage (inset of Fig. 7d). This property not only indicates a high power conversion efficiency from the pump to microcombs, but enables the soliton crystals formed stably through adiabatic pump-laser scans, without the need for the complex techniques used in other demonstrations of Kerr solitons to avoid dissipation of the solitons due to thermal changes suffering from sudden drop in intracavity power.

Evolving from the MI state, soliton crystals exhibit various states because of different soliton arrangements, resulting in many unique “palm-like” spectra in the frequency domain, such as the perfect, Schottky defects, Frenkel defects, disorder, superstructure, and irregular states^{88,118}. Among these soliton-crystal states, the perfect soliton crystal (PSC) is their simplest and most ideal representative, defined as all solitons evenly distributed within the resonators, as shown in Fig. 7a. In contrast to other soliton crystals with defects, the behavior of PSCs is unperturbed by missing or shifted soliton pulses, such a high regularity leading to a pure microcomb consisting of a few lines with a spacing of N (or X in Fig. 7a, which is the soliton number of PSCs) times of FSR. Accordingly, the multiplicity of soliton repetition rate superimposed on the increase in the number of solitons boosts the power of each comb line by N^2 (or X^2) times in comparison to the single-soliton state^{70,85}, as shown in Fig. 7c, d. The enhanced comb lines offer promise for a number of applications requiring high-power comb lines, ranging from optical coherent communications to astrophysical spectrometer calibration. Furthermore, PSCs could be regarded as a single-soliton state with a multiple FSR reaching terahertz in a common resonator circumvents the bending losses and dispersion control for extremely small microresonators.

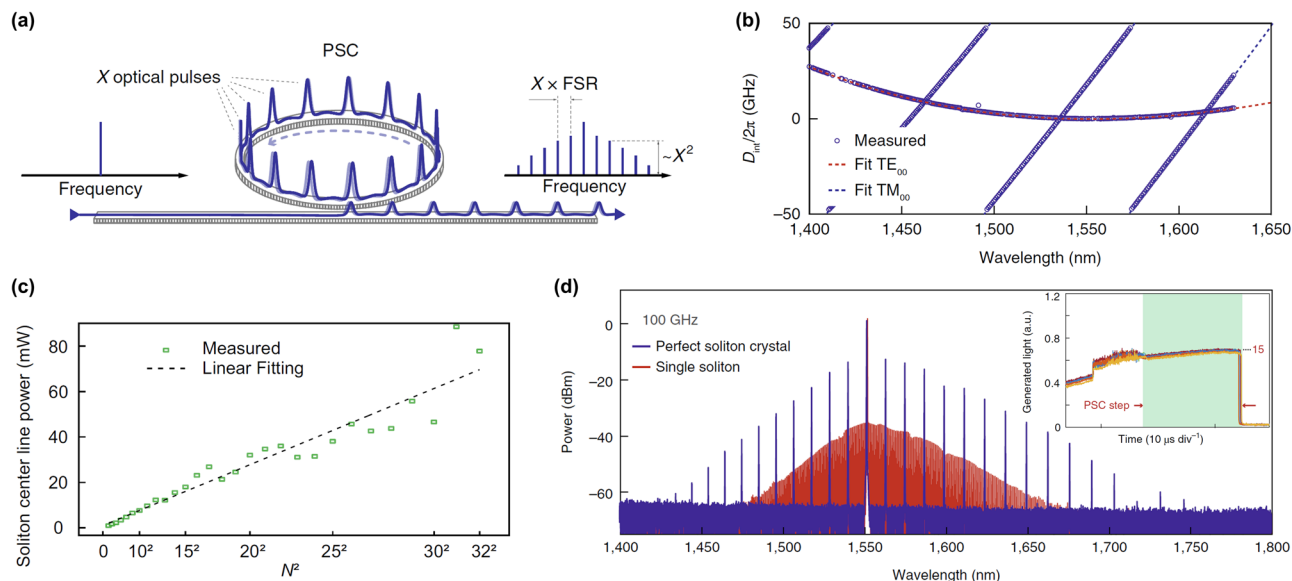


Fig. 7 | PSCs in Kerr microresonators. **a** Principle of the PSC consisting of X pulses formed in the CW-driven Kerr microresonator⁷⁰. **b** Measured integrated dispersion of a SiN microresonator (blue circles) and the fitting curves for the fundamental transverse electric (TE; red dashed curve) and transverse magnetic (TM; blue dashed curves) mode families. The cross points between such two mode families would occur avoided mode crossings (AMXs)⁷⁰. **c** The soliton center line power extracted from experimental spectral envelopes versus the square of soliton number N^2 in

PSC⁸⁵. **d** Optical spectra of PSC state containing 15 solitons (blue lines) and single-soliton state (red lines) in a SiN microresonator device under the same conditions of the pump power and effective detuning. The inset shows five repeated scan transmission traces, the PSC states with a soliton number of 15 are highlighted by the green background⁷⁰. Images are adapted with permission from refs. 70,85. Copyright 2019, 2021 Springer Nature Limited.

After demonstrating the generation of PSCs, a significant amount of effort has been made to obtain deterministic PSC states and controllable switching between different PSC states. In general, excitation of a PSC state is often random, since the regular distribution of solitons is easily interfered by the thermo-optic nonlinearity. Hence, accessing PSCs requires a delicate tuning process in the parameter space of pump power and detuning. Research on the dynamic of PSCs has demonstrated the generation of PSCs is typically achieved at relatively low pump powers in comparison with the standard procedures of multi-soliton excitation⁷⁰. Below the power threshold, the microresonators featured with AMXs exhibit a long PSCs step, indicating the systems for PSCs are robust and reproducible (as shown in inset of Fig. 7d). By varying the pump resonances to adjust the modulated CW background aided by AMXs, PSCs with different soliton numbers were achieved¹¹⁶, as presented in Fig. 8a, b. The controllable switch between different PSC states offers a convenient approach for tuning the repetition rate of soliton microcombs in a monolithic device. Furthermore, this technique was promoted by combining photorefractive effect⁴⁹, thermo-optic effect¹¹⁸, and auxiliary-laser-assistance¹¹⁹. However, suffering from the complex soliton dynamics and the weak AMX-induced modulation on CW background, the soliton numbers of PSCs do not exactly align with the relative resonance shifts between pumping modes and AMXs, as shown in Fig. 8b. This discrepancy hinders the flexible switching of the PSC states. In order to address this issue, a pumping scheme consisting of two CW lasers was proposed to manipulate PSC states directly⁸⁵. The principle of synthesized PSCs generated in a microresonator driven by dichromatic pumping is presented in Fig. 8c, d, where a strong periodic modulation is formed due to the beating of two pump lasers, offering an artificial background potential field to evenly trap solitons in distribution. By controlling the beating of dichromatic pumping, the reconfigurable PSCs with soliton numbers from 1 to 32 were synthesized in a monolithic silica glass microresonator, as shown in Fig. 8d. Such a highly ordered temporal distribution could coherently enhance the PSC-comb lines power up to 3 orders of magnitude compared with

the single-soliton state. In a certain sense, this technique could be regarded as an extremely simple pulsed pump containing two comb lines with a repetition rate is an integral harmonic of cavity FSR.

Along with the research on accessing and switching PSCs, the high conversion efficiency of soliton crystals has been demonstrated in several investigations. In one experiment by Corcoran et al., a defective soliton crystal with an internal conversion efficiency of 42% was demonstrated and used as a single integrated chip source in wavelength-division multiplexed (WDM) system². By leveraging the high stability and coherence of soliton crystals, an ultrahigh bandwidth optical transmission with 44.2 Tbps using 64 quadrature amplitude modulation (QAM) was demonstrated. Furthermore, another defective soliton crystal was demonstrated experimentally and numerically in a SiN microresonator for the first time, which has a flat top and a conversion efficiency $\sim 10\%$ ¹²⁰. A more recent demonstration by Weng et al. realized the tunable switching soliton states of single-soliton, 2-PSC, and 3-PSC with a conversion efficiency of 7.7%, 11.4%, and 13.5%, respectively, in a dispersion-engineered dual-mode microresonator⁹⁰. Benefitting from the enhanced comb lines of PSCs, both PSCs exhibited broadband spectra exceeding an octave-spanning range from 127 THz to 270 THz. Following this demonstration, the same research group showed the versatility of octave-spanning PSCs with higher conversion efficiency in a SiN microresonator. By optimizing the power coupling coefficient, a series of different PSCs driven by different pump resonances achieved conversion efficiencies above 50%¹²¹. In addition to the results mentioned above, there are several investigations on microcombs with high conversion efficiency in soliton crystal states have been realized by other schemes. We will discuss these specifically in following sections.

Dark soliton microcombs

In contrast to the DKS requires the optical cavity to display anomalous dispersion at the pump wavelength, dark soliton is a type of localized stationary structure found in cavities operating in normal dispersion regime, which is consistent with the inherent material dispersion of most photonics platforms, thereby reducing the requirements on the geometry of resonators for generating microcombs¹²². Accordingly, the phase-matching of the MI process is not satisfied for normal-dispersion microresonators, which is

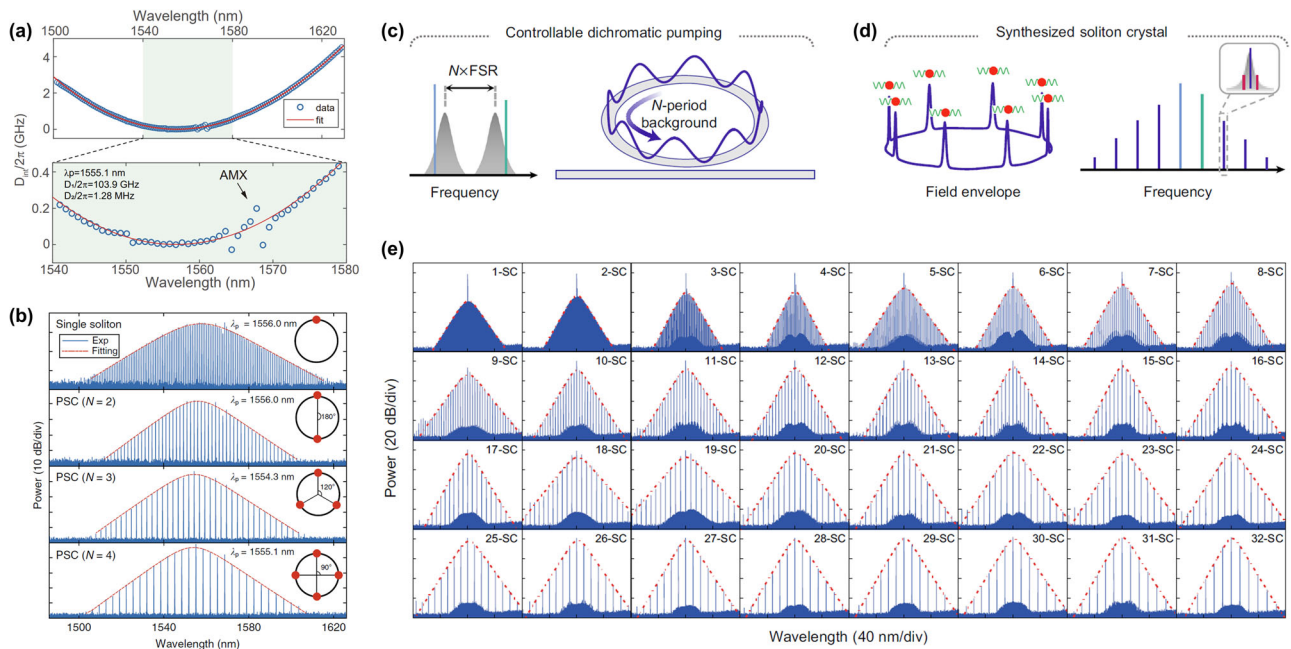


Fig. 8 | Deterministic accessing PSC states through AMX and controllable dichromatic pumping. **a** Measured integrated dispersion of the fundamental TE mode family in a SiN microresonator (top) and zoom-in of region between 1540 nm and 1580 nm (bottom). Blue circles show the measured integrated dispersion and the red line shows its fitting curve. The AMX is marked around the wavelength of 1565 nm¹¹⁶. **b** Optical spectra (blue lines: experiment; red lines: sech^2 fitting) of single-soliton state and three deterministic PSC states ($N = 2, 3, 4$) generated at the resonances of 1556.0, 1554.3, and 1551.1 nm, respectively. The insets illustrate soliton distribution inside the microresonator¹¹⁶. **c** Conceptual schematic for

deterministic PSC by using dichromatic pumping. The beating of the dual-wavelength lights (blue and green lines) constructs a traveling periodic modulated background and trapped soliton to form PSC⁸⁵. **d** Synthesized PSC in the dichromatic pumped system with a sech^2 envelope in the spectrum. The vibration of soliton will induce modulated sidebands around the main comb lines (inset)⁸⁵. **e** Measured optical spectra for 1–32 synthesized SC with smooth sech^2 envelopes (red dashed lines)⁸⁵. Images are adapted with permission from refs. 85,116. Copyright 2020 Springer Nature Limited.

necessary to trigger the state of mode-locked microcombs⁸⁸. To avoid excitation of dark pulses under a large red-detuning in the thermally unstable regime, several excitation methods have been proposed to enable the formation of dark solitons in the normal dispersion regime, such as AMX^{65,75}, amplitude-modulated optical pumping^{123,124}, pulsed pumping^{53,101–105}, double-cavity coupled photonic dimers^{40,86}, and photonic crystal microcavity (PhCR)^{92,125}. Among these methods, AMX is the most prevalent approach for generating a normal-GVD comb. In contrast to the detrimental effect on soliton generation in the anomalous GVD regime⁸¹, the mode coupling between different mode families in normal-dispersion microresonators causes a shifting of the coupled resonances and locally alters the dispersion to allow for MI. In the representative experiment with dark solitons, AMX was employed to initialize the MI, and then realized dark solitons in a SiN microresonator via a thermal-tuning method. The measured integrated dispersion disturbed by AMX is presented in Fig. 9a³⁹. The pump frequency is gradually tuned from the blue side of a resonance, the power transmission trace is depicted in Fig. 9b. It is notable that the whole tuning range is almost exclusively located in the effectively blue-detuned regime, that implies the intracavity pump field stays on the upper branch of the bistability curve, in which MI is weak or even disappeared. The optical spectra and intensity noise at different detuning stages are presented in Fig. 9c, d, where the low-noise mode-locking microcombs with flat and modulated envelopes were observed in the power drop step regime, indicating the existence of a state transition similar to the soliton step in anomalous GVD regime. Benefitting from the weak MI and the blue-detuned pump, the generation of dark solitons follows a deterministic pathway (Fig. 9b) and exhibits a robust character similar to PSC. The corresponding pulse profile of the normal-GVD comb is presented in Fig. 9e, it is a complex structure depicted as low-intensity oscillations embedded in a high-intensity background. Different from the isolated ultrashort pulses with time-bandwidth-product limited durations in the anomalous dispersion region, dark solitons are the chirped pulses far from the Fourier-

transform limitation, which can be interpreted as two stably interlocked SWs, connecting the upper and lower homogeneous steady-state solutions of the bistable cavity response⁷⁶. These localized waveforms exhibit wide pulse durations, the large duty cycle analogous to square waves indicates high conversion efficiency, as proven in various following researches. The key benefits of dark soliton in the normal GVD regime, including ease access, high stability, high conversion efficiency, and slower power falloffs in spectrum, make it a more ideal light source for applications.

Dark pulse shares many similar properties with its counterpart in the anomalous GVD regime in response to parameters of Kerr resonators. For example, a small dispersion coefficient and large nonlinear coefficient result in a broad spectral bandwidth and low conversion efficiency; the increase of power coupling coefficient accompanies an increase in conversion efficiency at the expense of a decrease in Q factor; a large FSR of cavity would enhance the intensity of comb line and boost the conversion efficiency. In contrast, the evolutionary dynamics of dark soliton with respect to detuning are unique. Using the setup as shown in Fig. 10a, Nazemosadat et al. revealed the switching dynamics of dark-pulse in a Kerr microresonator by forward and backward tuning method¹²⁶. Figure 10b presents a measured a transmission trace under a fixed pump power. As the pump laser is swept forward into resonance, the comb power increases in a gradual manner while displaying continuous steps in consistent with Fig. 9b. After accessing the maximum detuning of dark pulse in the forward tuning, the comb power drops along the same trace in the reverse direction by tuning the pump backward. Furthermore, the comb power continually drops in a smoothed, steplike pattern in further backward tuning until the pump non-resonant completely. The evolution of comb power in the forward and backward pump tuning shows hysteresis behavior, similar to what has been observed for bright solitons in anomalous-dispersion resonators. The optical spectra and their corresponding simulated intracavity pulse profiles at different detuning stages, marked in Fig. 10b, are shown

Fig. 9 | Dark pulses in a normal-dispersion microresonator. **a** Measured integrated dispersion with respect to the resonance around 1537.4 nm. Red circles, cold cavity; blue crosses, pumped cavity with pump power of ~1 W. **b** Power transmission traces when pump swept across a resonance. 20 measured traces are overlapped with different colors to show reproducibility. **c, d** Optical spectra and radio-frequency spectra (blue lines, red lines indicate the noise floor) for each stage marked in (b). **e** Measured (top) and simulated (bottom) cross-correlation for the comb shown in (c), III. Images are adapted with permission from ref. 39. Copyright 2015 Springer Nature Limited.

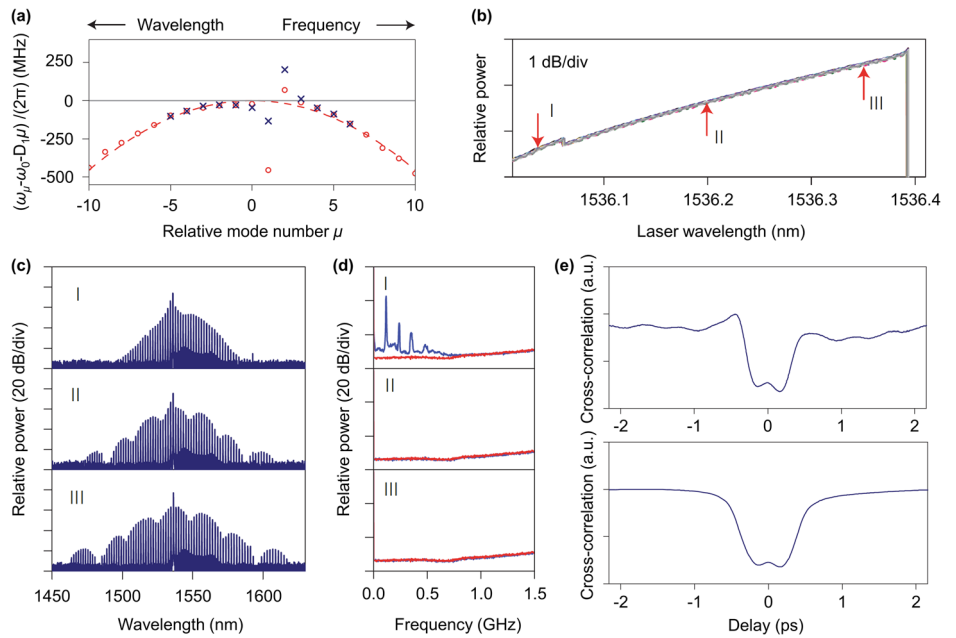
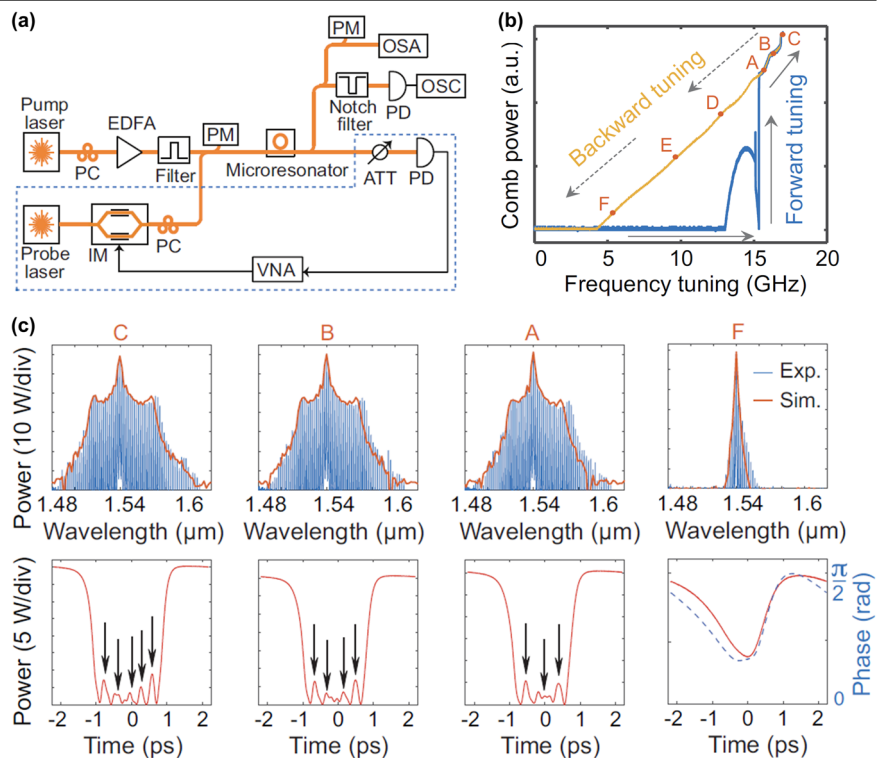


Fig. 10 | Deterministic switching of dark pulses. **a** Setup for normal-comb generation and measurement. **b** Measured comb power when the pump scans forward (blue line) then backward (yellow line). **c** Optical spectra at different pump detuning marked in (b). The comb envelope of each state is simulated and shown in red lines, the corresponding simulated temporal profiles are presented in the bottom panels. The arrows point the number of low intensity oscillations. For state F, the phase of the pulse is shown in dashed blue line. OSC Oscilloscope, ATT Attenuator, VNA Vector network analyzer. Images are adapted with permission from ref. 126. Copyright 2021 American Physical Society.



in Fig. 10c. The optical spectra depicted similar normal-GVD combs except for the variation of bandwidth in parallel with comb power evolution. Strikingly, the simulated waveforms revealed the switching of low intensity oscillation at the center of the dark-pulse structure, as the arrows pointed in Fig. 10c. The number of low-intensity oscillations increases as the comb power increases in forward pump tuning, while vanishing one by one in the reverse direction. In bifurcation analysis, these temporal structures arise from the different snaking branch solutions of SWs; the orders of SWs and their stable regimes decrease with increasing detuning, thus called the collapsed snake structure⁷⁶. When the ratio of low-intensity structure is larger than high intensity, a

flat-top pulsed structure called platicon is formed and deemed as a bright pulse evolving from a dark pulse in normal dispersion regime, which is a higher-order dark pulse can be accessed at the stable Maxwell point in bifurcation analysis^{76,127}. Intuitively, a dark pulse can be regarded as the inverse bright multi-solitons with a coherently assembled structure embedded in a high-intensity constant background, where the low-intensity ripples correspond to the pulse peaks of assembled solitons. Therefore, dark pulses present modulated spectral envelopes and high conversion efficiencies similar to multi-soliton, and a reproductive pathway free from the disordered distribution of multiple solitons in microresonators. In addition, the maximum comb power is consistent

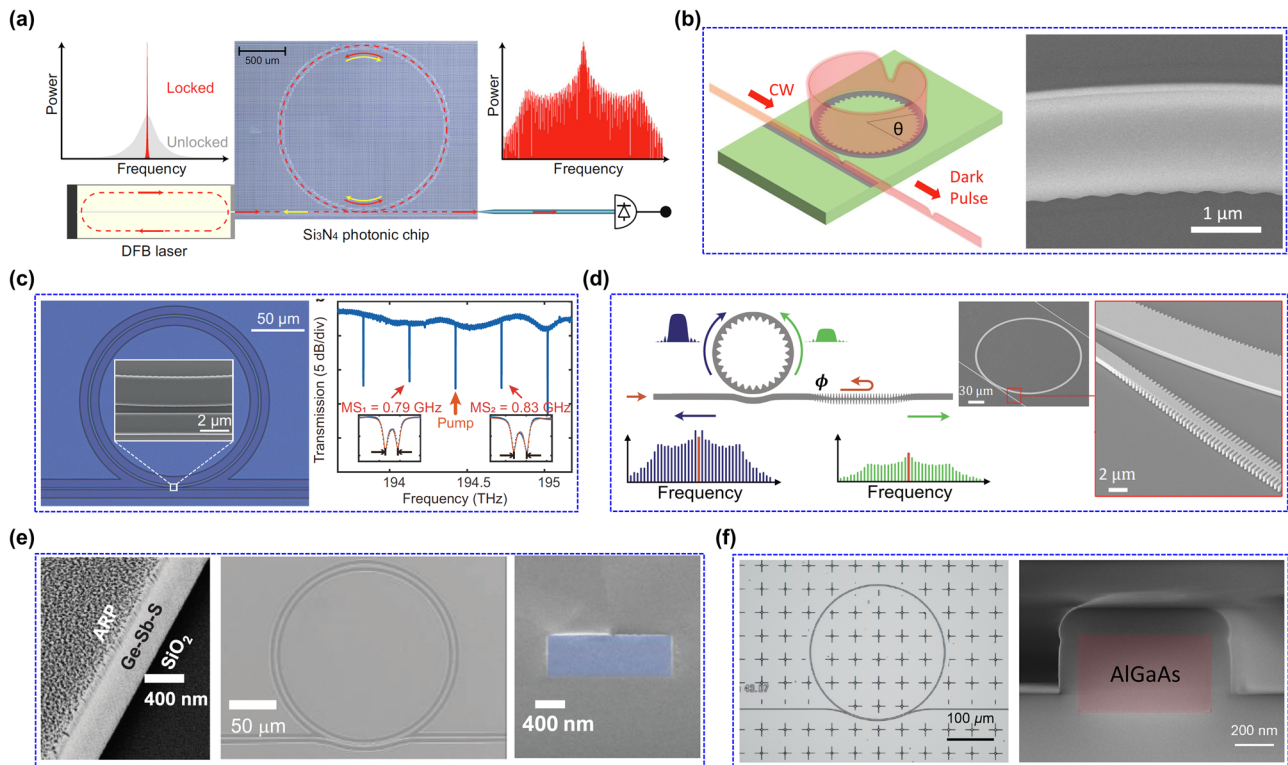


Fig. 11 | Dark pulses with high conversion efficiency generated on different platforms. **a** Schematic of platicon generation using a DFB laser self-injection-locked to a photonic chip-based, high-Q SiN microresonator¹²⁸. **b** Illustration of dark pulse generation in the tantala (Ta_2O_5) PhCR (left), and the scanning-electron-microscopy (SEM) image showing a section of the PhCR (right)¹²⁵. **c** Microscope photograph of a SiN microresonator with inner and outer angular gratings (left), and the measured transmission spectrum around the pump wavelength 1542 nm. The arrows indicate two mode splittings (MS_1 and MS_2 , red) occurring around the pump (orange arrow; right). Insets show the SEM image of the coupling section of the microresonator and the magnified views of the arrowed modes¹³⁰. **d** Schematic of the dark pulses generation with high conversion efficiency in a PhCR with a coupling

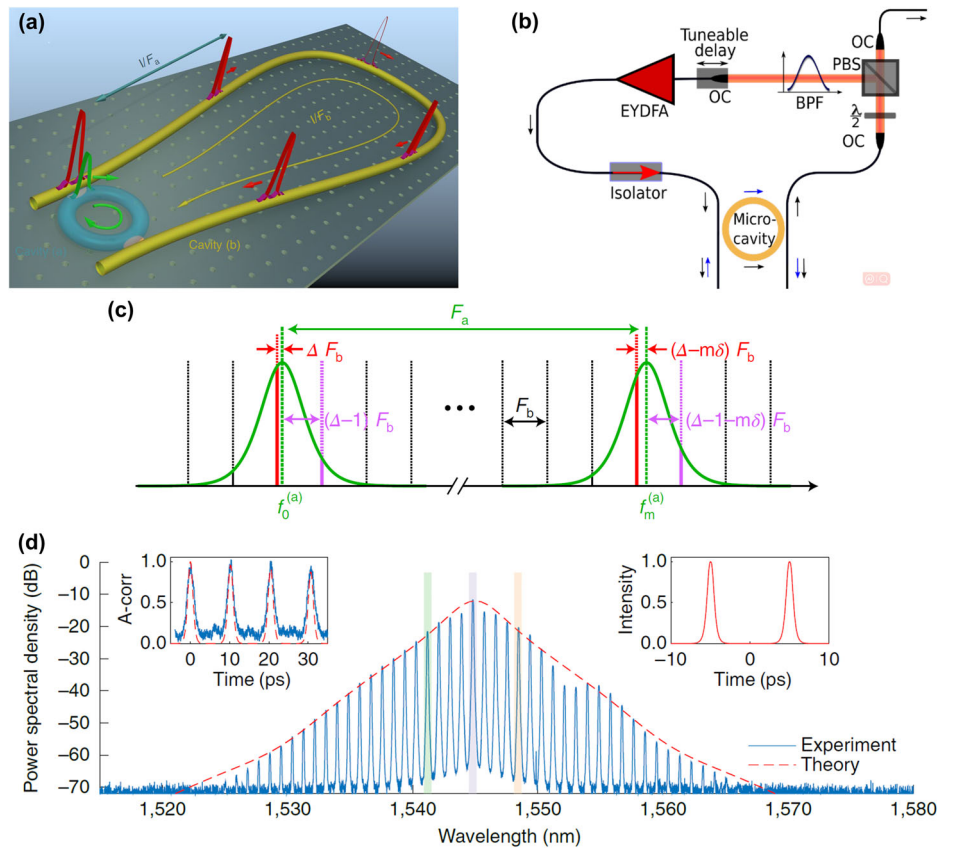
waveguide reflector (left), SEM image of the fabricated Ta_2O_5 PhCR and waveguide reflector (middle), and the magnified views of the coupling waveguide reflector section (right)⁹². **e** SEM images of sidewall of a chalcogenide glass (GeSbS) waveguide (left), GeSbS microresonator (middle), and the cross-section with a silica cladding waveguide (right), respectively. ARP is a photoresist named ARP-6200¹³¹. **f** Microscope photograph of one AlGaAsOI microresonator (left), and the SEM image of the cross section of the microresonator. The AlGaAs core is highlighted in red, and silica forms the substrate and cladding (right)¹³². Images are adapted with permission from refs. 92,125,128,130–132. Copyright 2022, 2023 Springer Nature Limited. Copyright 2023 Wiley-VCH GmbH. Copyright 2023 SPIE and under Creative Commons Attribution from arXiv.

with the duration of dark pulse or the number of low-intensity ripples, which is determined by the Maxwell point related to the parameters of the system, and is similar to the limitation of the maximum soliton numbers confined in a resonator.

Encouraged by the various advantages of dark solitons, a number of platforms for generating dark soliton microcombs with high conversion efficiency have been studied. For instance, Lihachev *et al.* used laser self-injection locking to demonstrate a fully integrated platicon microcomb operating at a microwave K-band repetition rate¹²⁸. By using a high-Q SiN microresonator self-injection-locked by a DFB laser (Fig. 11a), multiplaticon states with low phase noise were excited directly without sophisticated active control. The formation dynamics and properties of platicons were investigated, in which a high conversion efficiency of 40% was demonstrated. In addition, the same configuration was adapted to demonstrate hertz-linewidth semiconductor lasers using CMOS-ready ultra-high-Q microresonators, where a self-injection-locked platicon microcomb with low phase noise and narrow linewidth is obtained⁵⁹. Another approach to excite dark pulse in normal dispersion regime is by using PhCR. A PhCR is a microresonator with periodic modulation to create frequency-domain point defects¹²⁹, which can locally modify the dispersion akin to AMXs to enable MI. By employing an edge-less tantala PhCR (as shown in Fig. 11b), Yu *et al.* showed the dark-to-bright continuum via controlling the strength of defect along with the pump-cavity detuning¹²⁵. They demonstrated flexible control over the bandwidth and conversion efficiency of microcomb, achieving a 200-GHz normal-GVD microcombs

spanning 180 ~ 210 THz with a conversion efficiency of 21%. Furthermore, Li *et al.* proposed a PhCR with a modulated structure on both the inner and outer edges of the microresonator (Fig. 11c) to generate stable, power-efficient normal-GVD microcombs with high spectral symmetry¹³⁰. The structure of such PhCR results in two symmetrically positioned local dispersion alterations on either side of the pump mode (Fig. 11c), eliminating the odd components of dispersion responsible for the asymmetry of dark-soliton microcombs. Moreover, by adjusting the interval between the positions of the dispersion alterations and the pump mode, deterministic perfect platicon crystals were achieved. In contrast to the PSCs in anomalous GVD regime, the conversion efficiency of microcombs increases slightly rather than linearly with the number of platicons due to the duration of the dark pulses further compressed within limited angular space. Here, a normal-GVD microcomb in a single-platicon case with a conversion efficiency of 27.6% was demonstrated. Recently, by using a pump-recycling photonic crystal reflector in the coupling waveguide (Fig. 11d), a measured 65% conversion efficiency and 97% pump consumption of a 40 mW input pump laser was demonstrated in an over-coupled PhCR with normal dispersion⁸⁸. Besides advances on excitation schemes of dark-soliton microcombs, optical materials with favorable properties provide another route to support microcombs with high conversion efficiency. Xia *et al.* demonstrated both a bright soliton-based microcomb with a bandwidth of 240 nm and a dark-soliton microcomb with a conversion efficiency of 21.8% in a single GeSbS microresonator in two fundamental polarized mode families (Fig. 11e)¹³¹. Alternatively, by using microresonators on an AlGaAs

Fig. 12 | Laser cavity solitons generation in microresonator nested into a gain fiber cavity.
a Principle of operation of microcomb laser cavity-soliton formation. A short pulse (green) propagates in the microcavity (blue) sustained by a longer pulse (red) and a weak higher-order ‘super-mode pulse’ (purple) in the gain fiber loop (yellow).
b Experimental setup for laser cavity solitons generation. **c** Distribution of cold-cavity resonances. Microresonator resonances are represented in green, and the amplifying-fiber-loop resonances are in black, with leading and first-order supermodes highlighted in red and purple, respectively. The normalized frequency offset between the central frequency of the leading supermode and the microcavity resonance is Δ ; The variable δ is the normalized FSR detuning.
d Typical optical spectrum of laser cavity soliton, which contains two equidistant solitons in one round-trip. Insets: the measured autocorrelation traces (blue line in left inset) and simulated intensity profiles (dotted red dashed line in left inset and red solid line right inset). OC optical collimator, PBS polarizing beam splitter. Images are adapted with permission from ref. 72. Copyright 2019 Springer Nature Limited.



on-insulator platform (Fig. 11f), Shu et al. generated a dark-soliton microcomb with an unprecedentedly wide tuning range of over one free spectral range. The conversion efficiency reached $\sim 15\%$ ¹³². Combining the same configuration with foundry-based silicon photonics, dark-soliton microcombs were demonstrated to driven system-level data links. Such synergy of microcombs and other integrated components would facilitate the next generation of integrated photonics¹³³.

Laser cavity soliton microcombs

Recently, a novel bright dispersive soliton named laser cavity soliton was demonstrated in a microresonator nested into a pump-generating active ring cavity. The principle of laser cavity soliton is presented in Fig. 12a, which contains a Kerr microresonator and a longer amplifying fiber loop. The exact experimental setup is shown in Fig. 12b⁷². It is observed that the Kerr microcavity is embedded within a fiber loop assembled to resemble a mode-locked laser without a saturable absorber. The pulse propagating in the fiber loop is boosted and spectrally limited by the erbium-ytterbium co-doped fiber amplifier (EYDFA). By adjusting the length of the delay line, the resonance distribution of such two cavities is finely tuned to ensure only a single fiber cavity mode in each microresonator mode to prevent supermode instability (Fig. 12c). The pulse sustained in microresonator, and spectrally broadened by the Kerr nonlinearity over the laser-gain bandwidth. A tunable bandpass filter (BPF) is employed in the fiber loop to suppress excessive nonlinear phase shift and maintain the locked coherence of comb lines enabled by the FWM effect. The principle of such laser cavity soliton is similar to the filter-driven FWM laser, where a resonator is used as a filter as well as a nonlinear gain element in an erbium doped-fiber cavity¹³⁴. The measured optical spectrum of laser cavity soliton is presented in Fig. 12d, presenting a broadband comb with a unique envelope due to the interference between the fields in the two cavities. The pulse profiles both in experimental and theoretical revealed it is the bright-soliton combs (insets in Fig. 12d). Remarkably, the laser cavity soliton does not require the pump

background wave to maintain its existence (i.e., background-free), which releases most pump energy to be converted into comb modes. Compared to the conversion efficiency of a few percentage points for conventional bright soliton, here the laser cavity soliton achieved a conversion efficiency of 75%, with a theoretical maximum reached to 96%. Such high conversion efficiency, combined with the regular pulsed nature, motivates further pursuit of bright solitons. Very recently, Nie et al. deeply studied the laser cavity soliton generation and interaction dynamics in a FP-microresonator-filtered fiber laser, and demonstrated a self-starting soliton microcomb with a high conversion efficiency of 90.7%¹³⁵. Here the FSR of the employed FP-microresonator is ~ 10 GHz, the corresponding synchronous repetition rate of soliton is favorable for application in X-band. It is incomparable to conventional bright soliton limited by the corresponding large volume and low conversion efficiency. Besides the excellent conversion efficiency, it has been discovered that the microresonator-filtered fiber laser system exhibits a property of slow nonlinearity arising from the EDFA and the thermal response of the Kerr microresonator, which can transform the desired soliton state to be the dominant attractor of the system^{73,74,136,137}. Therefore, the self-emergence (i.e., self-starting) of specific soliton states and flexible switching between different states by tailoring the global parameters of the system were enabled. Moreover, the generated soliton states exhibited high stability and self-healing capability, which are desired merits for microcombs applied in practice.

Replacing the gain fiber loop in the microresonator-filtered fiber laser system by a passive waveguide, a novel hybrid Mach-Zehnder micro-ring resonator architecture was proposed to support soliton microcomb with high conversion efficiency. The principle of the proposed micro-ring resonator is presented in Fig. 13a, consisting of a Kerr microresonator for motivating DKs, embedded in a secondary cavity that acted as a feedback section⁸⁷. The optical path length of the secondary cavity was designed to be twice that of the microresonator, and can be delicately tailored and tuned (by microheater in the experiment as shown in Fig. 13b) to set a phase difference

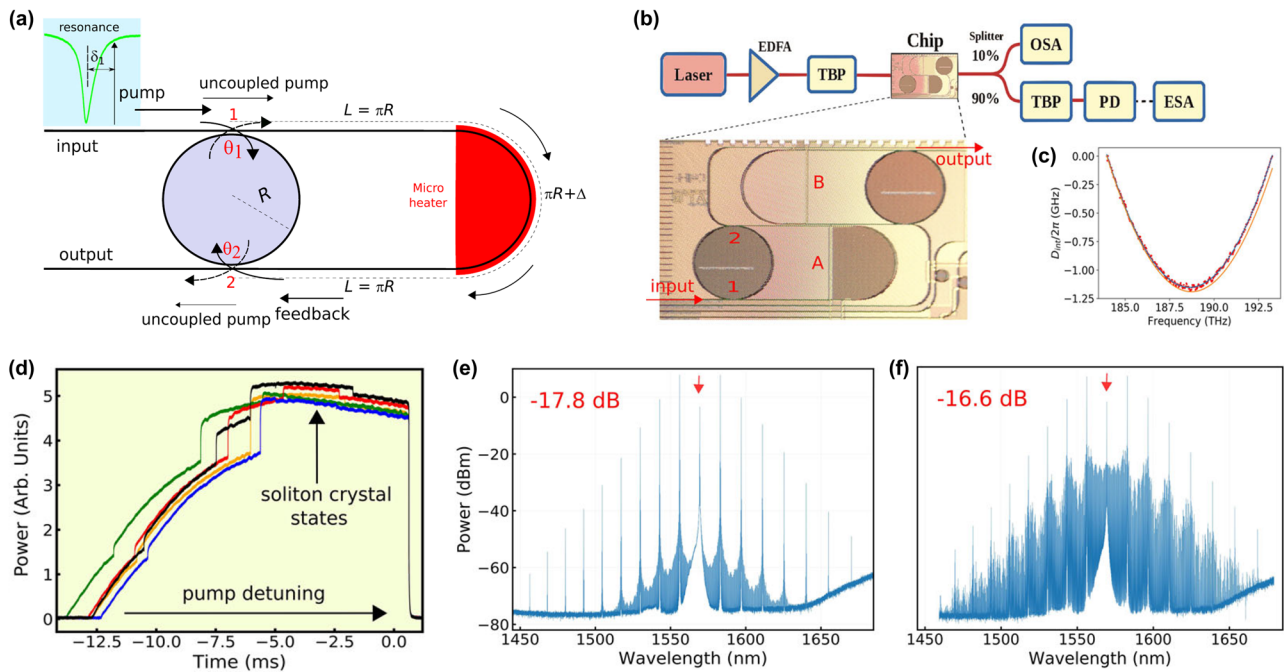


Fig. 13 | Efficient soliton-crystal microcomb generation in a microresonator with interferometric back-coupling. **a** Schematic of the ring resonator with an interferometric back-coupling architecture, where the ring is nested in a cavity twice its length. The pump-resonance detuning, δ_1 , is in general nonzero (inset). Therefore, at the coupling points 1 and 2, there is a fraction of the field that is in- or out-coupled, while the remaining fraction is reflected. The interference of fields is adjusted by tuning (with a microheater) the length of the feedback section by Δ . **b** Experimental setup and picture of a chip containing two ring resonators with feedback (A and B).

c Measured integrated dispersion of resonator labeled as A in (b). **d** Comb power versus the pump detuning, which presents various soliton crystal states. The different colors represent consecutive pump scanning through the resonance. **e, f** Optical spectra of microcombs in PSC and defective soliton crystal states, respectively. The pump modes are highlighted by red arrows, and the depletion values of pump modes are presented in red. TBP tunable bandpass filter. Images are adapted with permission from ref. 87. Copyright 2022 Springer Nature Limited.

of π between the pump fields out-coupled from the microresonator and through-passed from the feedback section at node 2. The opposite phases between the fields cause a sharp pump depletion, which indicates an extreme conversion efficiency into the comb lines. In theory, the interference of the fields permits an unprecedented pump depletion above 80% and a high conversion efficiency only limited by the necessarily remaining pump background field to sustain DKS operation in the resonators. Driving the fabricated device as shown in Fig. 13b using a CW-laser with the conventional frequency scanning method, Boggio et al. demonstrated various soliton crystal states with high conversion efficiency (Fig. 13d), featured by a deeply depleted pump mode with a weaker intensity in comparison with other supermodes in spectra, as shown in Fig. 13e, f. Here, a microcomb in PSC state with a conversion efficiency as high as $\sim 55\%$ was achieved. Although the solitons demonstrated here are less robust, its robustness can be improved by referring to other geometry of resonator with feedback^{138–140}. Meanwhile, combining the advantages of isolated pulse profiles and spectrally smooth envelopes of bright solitons, the ultra-efficient microcombs enabled by microresonator with an interferometric back-coupling architecture are suitable for various applications such as astronomy, spectroscopy, and telecommunication.

Microcombs in dual-cavity coupled microresonator

Expanded from the mode splitting caused by coupling between different polarization or spatial modes in an individual resonator, dual-cavity coupled microresonator architecture has recently emerged as a favorable alternative approach to generate normal-GVD microcombs with high conversion efficiency aided by AMX. The typical structure of the dual-cavity coupled microresonator is presented in Fig. 14a, which is composed of two linearly coupled cavities, main and auxiliary, with microheaters on top of one or both of them¹⁴¹. Because of the close proximity of the two similar microresonators, such an architecture also called photonic dimer or photonic

molecule. The transverse modes of the resonators evanescently couple with each other, leading to AMXs (Fig. 14b) and localized anomalous dispersion to initiate the formation of normal-GVD microcombs. In comparison with AMXs in an individual cavity, the photonic dimer is immune to the randomness of the AMXs' locations and coupling strengths⁴⁰. By controlling the gap between resonators, the coupling coefficient between modes can be easily controlled. Furthermore, the resonance locations of the coupling modes can be tuned separately via heating the resonators. The benefits of photonic dimer enable the generation of wavelength-tunable normal-GVD microcombs in multiple resonances (Fig. 14c), improve the robustness of normal-GVD microcombs, and eliminate other parasitic effects in conventional microresonator that support more than one mode.

The normal-GVD microcombs utilizing AMXs in photonic dimer were first demonstrated by ref. 40. By tuning the power applied to the microheater of the auxiliary ring, the position of the AMX was controlled, facilitating the deterministic generation of normal-GVD microcombs with selected repetition rates in a monolithic device. Almost simultaneously, the same configuration was employed with two anomalous-GVD resonators by ref. 142. They demonstrated a similarly controllable AMX and proved that it could improve the pump-to-comb conversion efficiency. Benefiting from advances in micro/nanofabrication technologies, the potential of the photonic dimer in promoting microcomb properties has been further unlocked. As shown in Fig. 15a–c, Kim et al. demonstrated turnkey normal-GVD microcombs in a SiN photonic dimer device driven by a CW fixed-frequency laser⁸⁶. The generated mode-locked normal-GVD microcombs exhibited a high conversion efficiency of 40.6%, and the power of comb lines was greatly enhanced (as presented in Fig. 15c), which is encouraging for applications requiring sufficient power per line, such as data transmission⁴. Furthermore, the normal-GVD microcombs with high conversion efficiency generated in different photonic dimers were proved to be synchronized and coherent combined for a 2.9 dB increase in comb power. The

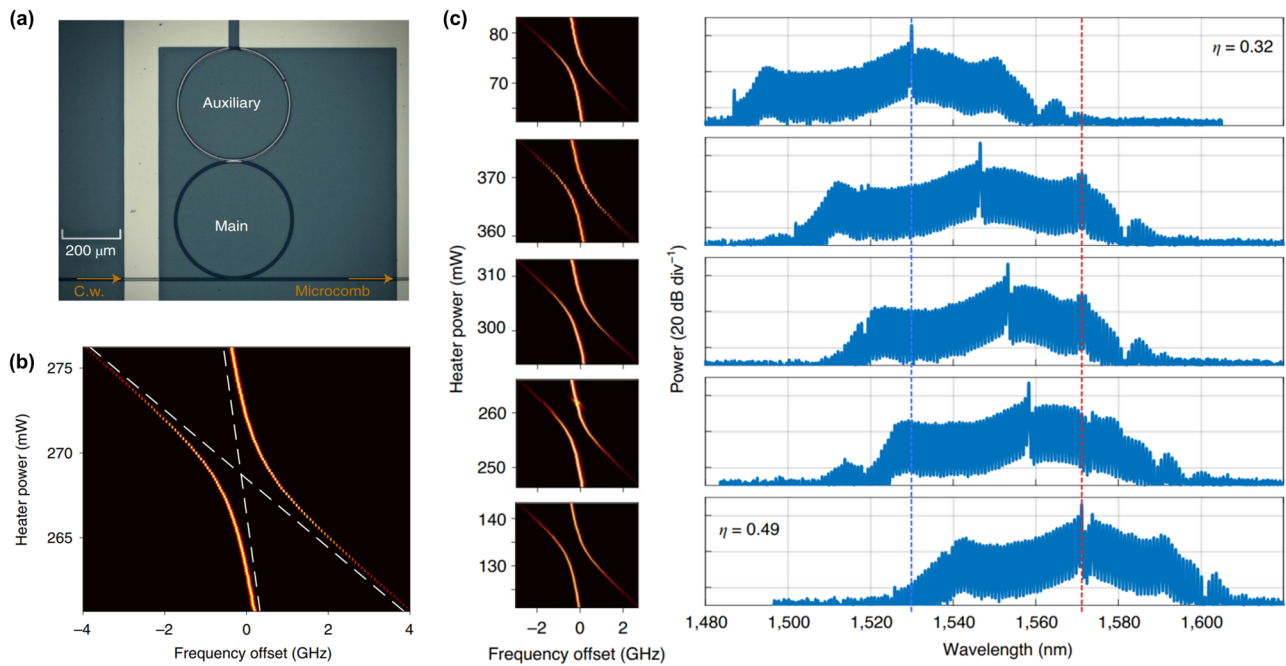


Fig. 14 | Dissipative soliton in a dual-cavity coupled microresonator.

a Microscope image of typical photonic dimer devices. A heater on top of the auxiliary microresonator controls the frequency location of the degeneracy point. **b** Transmission spectra versus heater power, showing the frequency split due to the coupling between resonances of resonators. **c** Wavelength-tunable microcombs

generated via selecting the frequency location of the split resonance. The dashed vertical lines indicate the center wavelength location of the initial (blue) and final (red) comb states. Images are adapted with permission from ref. 141. Copyright 2021 Springer Nature Limited.

spectral profiles were relatively flat while maintaining a high total conversion efficiency of 26%¹⁴³. It enables fully integrated systems to break the power limitation of an individual comb system. Taking advantages of the purity of the parameter space of photonic dimer, the normal-GVD microcombs can be robustly triggered in a broad range of existence. Figure 14c shows the broadly tunable normal-GVD microcombs achieved by selecting the frequency location of the split resonance. Remarkably, the conversion efficiency increased from 32 to 49% along with the increase in coupling rate at long wavelengths over the tuned frequency span¹⁴¹. The same configuration was further employed to generate a microcomb-based, widely and arbitrarily tunable laser source with a very narrow linewidth¹⁴⁴. More recently, a variant photonic dimer consisting of two anomalous-dispersion microresonators was demonstrated to generate bright Kerr solitons with high conversion efficiency¹⁴⁵. Figure 15d presents the microscopy image of the photonic dimer, in which the two linearly coupled cavities are significantly different in size. Both resonators have identical cross-sections, but the auxiliary resonator is smaller, resulting in a larger FSR that minimizes the interaction between cavities at longitudinal modes except the pump mode (Fig. 15e), which is responsible for the asymmetry and fluctuation of normal-GVD microcombs in similar-scale dual-cavity coupled microresonators. The pump is coupled into the main resonator and the pump resonance is shifted towards the red side with the perturbation of AMX while other resonances remain. Physically, this mechanism breaks the synchronization between pump mode and other comb-teeth modes that require a high red-detuning to reach soliton regime, allowing DKS microcombs with a high conversion efficiency under more sufficient pump coupling. As shown in Fig. 15f, a broadband bright soliton microcombs with a deeply depleted pump mode was demonstrated, achieving a conversion efficiency as high as 54%. It presents an order-of-magnitude improvement compared with conventional soliton microcombs in CW driven anomalous dispersion microresonators. Benefiting from the simple structure and relatively small footprint, it was proven to be suitable for wafer-level fabrication with high yield¹⁴⁶. Furthermore, the same architecture was applied in the normal dispersion regime, a wideband platonic microcomb with fewer spectral defects was generated and exhibited a conversion efficiency of 51%,

as shown in Fig. 15g¹⁴⁷. Besides the microcombs with high conversion efficiency aided by AMXs, photonic dimers were also demonstrated to support other emergent nonlinear phenomena, such as Fano-shaped dispersive waves and soliton hopping¹⁴⁸, which are not contained in a single-particle resonator and may further promote advance in integrated microcombs.

Accompanying the investigation on the photonic dimer, Xue et al. demonstrated an installation with two linearly coupled fiber cavities supporting soliton combs with ultrahigh conversion efficiency¹⁴⁹. Figure 16a illustrates the concept of super-efficient soliton generation in the mutually coupled optical cavities, where a normal dispersion resonator is coupled with an anomalous-GVD resonator. In contrast to the photonic dimers, where the auxiliary resonator served as an MI initiator or pump mode frequency shifter, the normal-GVD resonator is described as a storage unit that recycles the pump field, leading to a high-efficiency soliton microcombs generation in the anomalous-GVD resonator. Despite being limited by the high intrinsic loss of the fiber cavities and a relatively large dimension corresponding to an extremely low soliton duty cycle, the average soliton power measured was only 4.6×10^{-5} of the input pump power (Fig. 16b). An ultrahigh conversion efficiency close to 100% was numerically predicted for intrinsically lossless microcavities. It is an excellent paradigm promising a different route to generate microcomb with high conversion efficiency in integrated photonic dimers.

Summary and outlook

In this review, we presented an overview of the microresonator-based Kerr microcombs technologies that enable combs with high conversion efficiency. The reported Kerr microcombs with high conversion efficiency are summarized in Table 1. With the in-depth understanding of nonlinear physics, soliton states such as multi-soliton, soliton crystal, dark soliton, and laser cavity soliton can overcome the energy-conversion limitations of conventional single soliton in anomalous regime. Meanwhile, advances in micro/nanofabrication and photonic engineering capacity enable Kerr microcombs with high conversion efficiency generated with low loss, unprecedented topological architectures, and novel material platforms.

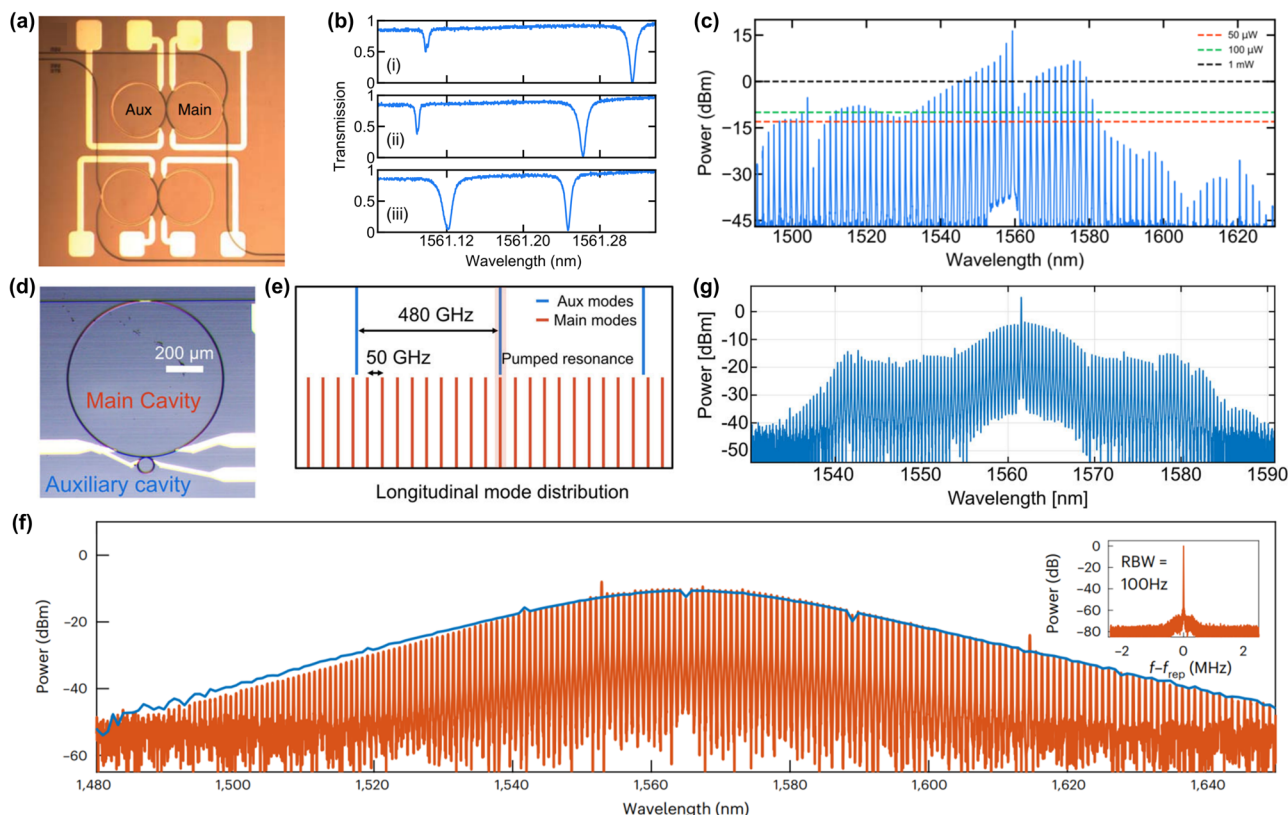


Fig. 15 | Efficient microcombs in dual-cavity coupled microresonators. **a** Image of dual-cavity coupled microresonators⁸⁶. **b** Transmission of device in different states. Split resonances (i) as the main ring heater is tuned, (ii) before parametric oscillation, and (iii) during comb generation⁸⁶. **c** Measured comb spectrum from automated generation with a comb line spacing of 201.6 GHz. Power levels of 50 μ W, 100 μ W, and 1 mW are given by red, green, and black dashed lines, respectively⁸⁶. **d** Image of photonic dimer devices with two dissimilar resonators¹⁴⁷. **e** Illustration of the longitudinal mode distribution of the main (orange) and auxiliary cavity modes (blue)¹⁴⁷. **f** Measured bright-soliton microcombs with high conversion efficiency (red) and simulated spectral envelope (blue). The inset shows the measured beat note signal between comb lines¹⁴⁵. **g** Optical spectrum of a platicon microcomb in a photonic dimer with two dissimilar resonators operating in the normal dispersion regime¹⁴⁷. Images are adapted with permission from refs. 86,145,147. Copyright 2019 Optica Publishing Group. Copyright 2023 Springer Nature Limited.

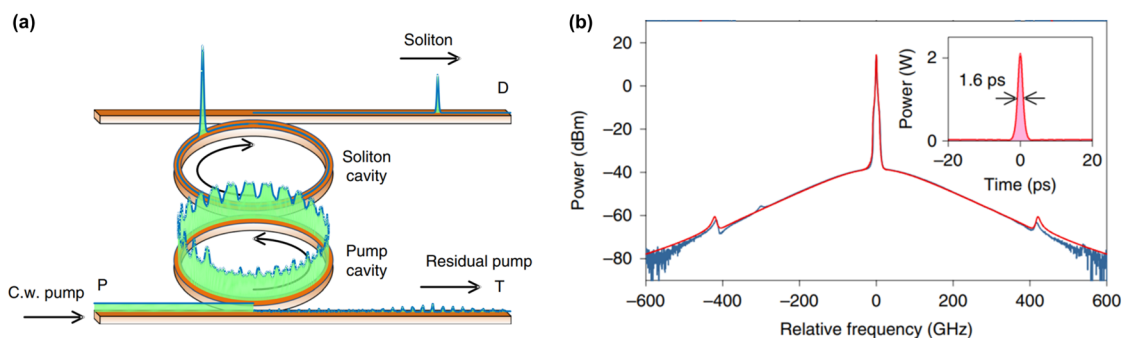


Fig. 16 | Super-efficient temporal solitons in mutually coupled optical cavities. **a** Illustration of soliton generation with pump recycling in mutually coupled cavities. The soliton circulates in a soliton cavity, while a pump cavity recycles the pump field to maximize energy transfer from the pump to the soliton. **b** Measured single-soliton microcomb in the soliton cavity (blue). Inset shows the simulated soliton pulse corresponding to the simulated microcomb (red line in the spectrum). The actually measured average soliton power is only 4.6×10^{-5} of the input pump power. Images are adapted with permission from ref. 149. Copyright 2019 Springer Nature Limited.

Aside from the impressive high conversion efficiency achieved by Kerr microcombs in recent advances, substantial obstacles remain in bringing these microcombs from laboratory into real-world applications. One critical problem is the level of integration. Although multi-soliton and dark soliton microcombs with high conversion efficiency have been demonstrated via the laser-injection locking method, a fully integrated photonic system remains a challenge due to the requirement of Kerr microresonator performance and the limited power of current on-chip lasers¹⁵⁰. Another key challenge is establishing a robust route to achieve the

desired Kerr microcombs with high conversion efficiency. As presented in the above section, current techniques for generating Kerr microcombs with high conversion efficiency mostly rely on complex servo systems to operate microcombs in desired states. Combining the rich dynamics involved in microcombs formation, the required monitoring and control capabilities for microcombs operation pose obstacles to full integration and deployment. Besides, the bandwidth and flatness of Kerr microcombs with high conversion efficiency obtained by current technologies are limited. While the comb-line power is enhanced due to the improvement

Table 1 | Summary of reported high conversion efficiency Kerr microcombs based on microresonators

Platform	FBR of MRR (GHz)	Dispersion type	Excitation method	Pump power (mW)	Comb state	Comb span (nm)	Conversion efficiency
SIN MRR ⁷⁷	~231	Normal	Intrinsic mode splitting	656	Dark soliton	~250	31.8%
Fiber FP resonator ⁸⁰	9.8	Anomalous	Pulsed pumping	3	Single-soliton	25	~5%
SIN photonic dimer ⁸⁶	200 and 206	Anomalous	Induced mode splitting	180	Non-soliton	150	40.6%
SIN MRR ⁸⁵	~1000	Anomalous	Intrinsic mode splitting	~800	Soliton crystal	Beyond an octave span	~50%
Hydex-resonator-filtered fiber laser ⁷²	~48.97	Anomalous	-	150	Laser cavity soliton	~50	75%
SIN MRR ⁹¹	105.2	Normal	Intrinsic mode splitting	350	Dark soliton crystal	~150	23%
SIN MRR ²⁶	229	Normal	Intrinsic mode splitting	363	Dark soliton	~120	25%
SIN MRR ⁹⁰	27.88	Anomalous	Pulsed pumping	60 and 620	Single-soliton	250 and 600	8% and 2.8%
SIN photonic dimer ⁴⁴	104.864 and 106.9	Normal	Induced mode splitting	13–18	Dark soliton	~80	32–49%
Hydex-resonator-filtered fiber laser ⁵⁷	48.9	Anomalous	-	80–120	Laser cavity soliton	~50	72%
SIN MRR ⁹⁷	~28.4	Anomalous	Intrinsic mode splitting	150	Soliton crystal	~250	55%
FP-resonator-filtered fiber lasers ³⁵	10.18	Anomalous	-	~600	Laser cavity soliton crystal	~60	90.7%
Ta ₂ O ₅ PhCR ³²	400	Normal	Frequency-domain point defect	100	Dark soliton	~250	>86%
SIN MRR ²⁰	103.02	Anomalous	Intrinsic mode splitting	300	Soliton crystal	~40	~10%
SiO ₂ microdisk resonator ²²	~22	Anomalous	Pulsed pumping	25 and 12	Single-soliton	~100	34% and a transient 54%
SIN MRR ⁸⁴	~150 and ~1000	Anomalous	Injection locking	~35 and ~40	Multi-soliton	~280 and beyond 400	25 and 40%
SIN MRR ⁹⁰	~1000	Anomalous	Intrinsic mode splitting	-	Soliton crystal	Beyond an octave span	7.7%, 11.4%, and 13.5%
SIN MRR ²⁸	26.2	Normal	Injection locking	~10	Platiton	~27	40%
AlGaAs MRR ³²	91	Normal	Intrinsic mode splitting	~150	Dark soliton crystal	~50	~15%
Ta ₂ O ₅ PhCR ²⁵	200	Normal	Frequency-domain point defect	33	Dark soliton	~240	21%
SiO ₂ microrod resonator ⁸⁸	~21 and ~105	Anomalous	CW laser frequency tuning	1.47 and -	Single-soliton	~15 and ~30	20 and 56%
Fiber FP resonator ⁹⁴	~1.84	Normal	Pulsed pumping	200	Platiton	~250	19%
Fiber FP resonator ⁹⁵	~10.21	Normal	Pulsed pumping	142	Platiton	~35	23.4%
SIN MRR ²¹	~1000	Anomalous	Intrinsic mode splitting	255	Soliton crystal	~1200	~50%
GeSiS MRR ¹³¹	~200	Normal for TE ₀₀ mode	Intrinsic mode splitting	33	Dark soliton	~80	~21.8%
2023 SIN PhCR ³⁰	298	Normal	Frequency-domain point defect	120–400	Platiton	~80	27.6%
2023 SIN photonic dimer ⁴⁷	480.4 and 49.97	Normal	Induced mode splitting	~47	Platiton	60	51%
SIN photonic dimer ⁵⁸	~19.96	Normal	Injection locking	30–40	Dark soliton	15	26%
SIN photonic dimer ⁴⁵	99.72 and 970	Anomalous	Induced mode splitting	7.4	Single-soliton	~160	54%
SIN photonic dimer ⁴⁶	99.7 and 380	Anomalous	Induced mode splitting	14.13	Single-soliton	~200	24–63%
SIN PhCR ⁵⁹	300	Anomalous	Frequency-domain point defect & Injection locking	21	Single-soliton	~130 and ~180	~10.5% and ~12.5%

MRR Microresonator, Hydex High-index doped silica.

of power conversion efficiency, the bandwidths of microcombs do not broaden significantly, which hinders the generation of stabilized microcombs facilitated by self-referencing technique. Meanwhile, the flatness of microcombs is not ideal due to the defective perturbations in the power distribution caused by additional nonlinear effects such as AMXs and stimulated Raman scattering. Furthermore, a majority of the reported Kerr microcombs with high conversion efficiency are focused on communication bands. However, there is a significant demand for visible and mid-infrared microcombs in the fields of chemical/biological sensing and molecular spectroscopy. The bandwidth of visible microcombs is quite limited, and the conversion efficiency is low¹⁵¹. Moreover, there are no reports yet about mode-locked mid-infrared microcombs with high conversion efficiency based on Kerr microresonators.

Despite there being numerous challenges for current techniques in generating Kerr microcombs with high conversion efficiency, the current trend of integrated optics remains a promising path that can be extended to achieve the desired goal. On the one hand, there are amounts of emerging nonlinear physics phenomena that require further investigation^{111,148,152}. With a broader insight beyond current focuses, it is anticipated that more favorable Kerr microcombs will be obtained based on new mechanisms. On the other hand, microcavities are yet to be thoroughly developed and understood. For instance, there is still great potential to further improve the performance of Kerr microcombs in the microresonators with higher *Q* values. Besides, there are several microcombs generated with high conversion efficiency in novel material platforms with both Kerr nonlinearity and second-order nonlinearity, which is beneficial for microcombs with extraordinary nonlinear dynamics in the visible band^{153–155}. In summary, there is an anticipating margin on the material platform to improve the performance of microcombs until it reaches the ultimate capabilities of microresonators. Along such two separated development routes, there are many open questions to be studied and answered. It is encouraging to see that this field has become an active field in optics today, and we foresee that there will be more achievements in the future that will make Kerr microcombs with high conversion efficiency the cornerstone in the next-generation integrated photonics. Over the next decade, we anticipate that the synergy between Kerr microcombs and their expanded applications will lead to further exciting breakthroughs in improving the microcombs' performance and promote the widespread deployment of microcombs, accelerating the transition of this technology into commercial production.

Received: 26 February 2024; Accepted: 26 June 2024;

Published online: 17 July 2024

References

- Hu, H. & Oxenlowe, L. K. Chip-based optical frequency combs for high-capacity optical communications. *Nanophotonics* **10**, 1367–1385 (2021).
- Corcoran, B. et al. Ultra-dense optical data transmission over standard fibre with a single chip source. *Nat. Commun.* **11**, 2568 (2020).
- Geng, Y. et al. Coherent optical communications using coherence-cloned Kerr soliton microcombs. *Nat. Commun.* **13**, 1070 (2022).
- Rizzo, A. et al. Massively scalable Kerr comb-driven silicon photonic link. *Nat. Photonics* **17**, 781–790 (2023).
- Rizzo, A. et al. Petabit-scale silicon photonic interconnects with integrated Kerr frequency combs. *IEEE J. Sel. Top. Quantum Electron.* **29**, 3700120 (2023).
- Trocha, P. et al. Ultrafast optical ranging using microresonator soliton frequency combs. *Science* **359**, 887–891 (2018).
- Suh, M.-G. & Vahala, K. J. Soliton microcomb range measurement. *Science* **359**, 884–887 (2018).
- Lukashchuk, A., Riemensberger, J., Karpov, M., Liu, J. & Kippenberg, T. J. Dual chirped microcomb based parallel ranging at megapixel-line rates. *Nat. Commun.* **13**, 3280 (2022).
- Yu, M. et al. Silicon-chip-based mid-infrared dual-comb spectroscopy. *Nat. Commun.* **9**, 1869 (2018).
- Stern, L. et al. Direct Kerr frequency comb atomic spectroscopy and stabilization. *Sci. Adv.* **6**, eaax6230 (2020).
- Suh, M.-G., Yang, Q.-F., Yang, K. Y., Yi, X. & Vahala, K. J. Microresonator soliton dual-comb spectroscopy. *Science* **354**, 600–603 (2016).
- Dutt, A. et al. On-chip dual-comb source for spectroscopy. *Sci. Adv.* **4**, e1701858 (2018).
- Newman, Z. L. et al. Architecture for the photonic integration of an optical atomic clock. *Optica* **6**, 680–685 (2018).
- Beloy, K. et al. Frequency ratio measurements with 18-digit accuracy using a network of optical clocks. *Nature* **591**, 564–569 (2021).
- Newman, Z. L. et al. Architecture for the photonic integration of an optical atomic clock. *Optica* **6**, 680–685 (2019).
- Nakamura, T. et al. Coherent optical clock down-conversion for microwave frequencies with 10^{-18} instability. *Science* **368**, 889–892 (2020).
- Liang, W. et al. High spectral purity Kerr frequency comb radio frequency photonic oscillator. *Nat. Commun.* **6**, 7957 (2015).
- Weng, W. et al. Spectral purification of microwave signals with disciplined dissipative Kerr solitons. *Phys. Rev. Lett.* **122**, 013902 (2019).
- Kwon, D., Jeong, D., Jeon, I., Lee, H. & Kim, J. Ultrastable microwave and soliton-pulse generation from fibre-photonic-stabilized microcombs. *Nat. Commun.* **13**, 381 (2022).
- Zhu, C. et al. Silicon integrated microwave photonic beamformer. *Optica* **7**, 1162–1170 (2020).
- Tan, T. et al. Predicting Kerr soliton combs in microresonators via deep neural networks. *J. Lightwave Technol.* **38**, 6591–6599 (2020).
- Xu, X. et al. Photonic perceptron based on a Kerr microcomb for high-speed, scalable, optical neural networks. *Laser Photonics Rev.* **14**, 2000070 (2020).
- Obrzud, E. et al. A microphotonic astrocomb. *Nat. Photonics* **13**, 31–35 (2019).
- Suh, M. G. et al. Searching for exoplanets using a microresonator astrocomb. *Nat. Photonics* **13**, 25–30 (2019).
- Caspani, L. et al. Multifrequency sources of quantum correlated photon pairs on-chip: a path toward integrated Quantum Frequency Combs. *Nanophotonics* **5**, 351–362 (2016).
- Wu, B.-H., Alexander, R. N., Liu, S. & Zhang, Z. Quantum computing with multidimensional continuous-variable cluster states in a scalable photonic platform. *Phys. Rev. Res.* **2**, 023138 (2020).
- Yang, Z. et al. A squeezed quantum microcomb on a chip. *Nat. Commun.* **12**, 4781 (2021).
- Joshi, C. et al. Frequency-domain quantum interference with correlated photons from an integrated microresonator. *Phys. Rev. Lett.* **124**, 143601 (2020).
- Kippenberg, T. J., Gaeta, A. L., Lipson, M. & Gorodetsky, M. L. Dissipative Kerr solitons in optical microresonators. *Science* **361**, eaan8083 (2018).
- Herr, T. et al. Temporal solitons in optical microresonators. *Nat. Photonics* **8**, 145–152 (2014).
- Guo, H. et al. Universal dynamics and deterministic switching of dissipative Kerr solitons in optical microresonators. *Nat. Phys.* **13**, 94–102 (2017).
- Pavlov, N. G. et al. Soliton dual frequency combs in crystalline microresonators. *Opt. Lett.* **42**, 514–517 (2017).
- Lucas, E. et al. Spatial multiplexing of soliton microcombs. *Nat. Photonics* **12**, 699–705 (2018).
- Wang, H. et al. Direct tuning of soliton detuning in an ultrahigh-Q MgF₂ crystalline resonator. *Nanophotonics* **12**, 3757–3765 (2023).
- Yi, X., Yang, Q. F., Yang, K. Y., Suh, M. G. & Vahala, K. Soliton frequency comb at microwave rates in a high-Q silica microresonator. *Optica* **2**, 1078–1085 (2015).

36. Brasch, V., Geiselmann, M., Pfeiffer, M. H. P. & Kippenberg, T. J. Bringing short-lived dissipative Kerr soliton states in microresonators into a steady state. *Opt. Express* **24**, 29312–29320 (2016).
37. Brasch, V. et al. Photonic chip-based optical frequency comb using optical Cherenkov radiation. *Science* **351**, 357–360 (2016).
38. Joshi, C. et al. Thermally controlled comb generation and soliton modelocking in microresonators. *Opt. Lett.* **41**, 2565–2568 (2016).
39. Xue, X. et al. Mode-locked dark pulse Kerr combs in normal-dispersion microresonators. *Nat. Photonics* **9**, 594–600 (2015).
40. Xue, X. et al. Normal-dispersion microcombs enabled by controllable mode interactions. *Laser Photonics Rev.* **9**, L23–L28 (2015).
41. Ji, X. et al. Exploiting ultralow loss multimode waveguides for broadband frequency combs. *Laser Photonics Rev.* **15**, 2000353 (2021).
42. Zhou, H. et al. Soliton bursts and deterministic dissipative Kerr soliton generation in auxiliary-assisted microcavities. *Light Sci. Appl.* **8**, 50 (2019).
43. Zhang, S., Silver, J. M., Bi, T. & Del’Haye, P. Spectral extension and synchronization of microcombs in a single microresonator. *Nat. Commun.* **11**, 6384 (2020).
44. Zhang, S. et al. Sub-milliwatt-level microresonator solitons with extended access range using an auxiliary laser. *Optica* **6**, 206–212 (2019).
45. Lu, Z. et al. Deterministic generation and switching of dissipative Kerr soliton in a thermally controlled micro-resonator. *AIP Adv.* **9**, 025314 (2019).
46. Stone, J. R. et al. Thermal and nonlinear dissipative-soliton dynamics in Kerr-microresonator frequency combs. *Phys. Rev. Lett.* **121**, 063902 (2018).
47. Fujii, S. et al. Versatile tuning of Kerr soliton microcombs in crystalline microresonators. *Commun. Phys.* **6**, 1–8 (2023).
48. He, Y. et al. Self-starting bi-chromatic LiNbO₃ soliton microcomb. *Optica* **6**, 1138–1144 (2019).
49. He, Y., Ling, J., Li, M. & Lin, Q. Perfect soliton crystals on demand. *Laser Photonics Rev.* **14**, 6 (2020).
50. Obrzud, E., Lecomte, S. & Herr, T. Temporal solitons in microresonators driven by optical pulses. *Nat. Photonics* **11**, 600–607 (2017).
51. Cole, D. C. et al. Kerr-microresonator solitons from a chirped background. *Optica* **5**, 1304–1310 (2018).
52. Li, J. et al. Efficiency of pulse pumped soliton microcombs. *Optica* **9**, 231–239 (2022).
53. Macnaughtan, M., Erkintalo, M., Coen, S., Murdoch, S. & Xu, Y. Temporal characteristics of stationary switching waves in a normal dispersion pulsed-pump fiber cavity. *Opt. Lett.* **48**, 4097–4100 (2023).
54. Weng, W. et al. Gain-switched semiconductor laser driven soliton microcombs. *Nat. Commun.* **12**, 1425 (2021).
55. Pavlov, N. G. et al. Narrow-linewidth lasing and soliton Kerr microcombs with ordinary laser diodes. *Nat. Photonics* **12**, 694–698 (2018).
56. Raja, A. S. et al. Electrically pumped photonic integrated soliton microcomb. *Nat. Commun.* **10**, 680 (2019).
57. Shen, B. et al. Integrated turnkey soliton microcombs. *Nature* **582**, 365–369 (2020).
58. Xiang, C. et al. Laser soliton microcombs heterogeneously integrated on silicon. *Science* **373**, 99–103 (2021).
59. Jin, W. et al. Hertz-linewidth semiconductor lasers using CMOS-ready ultra-high-Q microresonators. *Nat. Photonics* **15**, 346–353 (2021).
60. Stern, B., Ji, X., Okawachi, Y., Gaeta, A. L. & Lipson, M. Battery-operated integrated frequency comb generator. *Nature* **562**, 401–405 (2018).
61. Ji, X. et al. Ultra-low-loss silicon nitride photonics based on deposited films compatible with foundries. *Laser Photonics Rev.* **17**, 2200544 (2023).
62. Yu, M. et al. Breather soliton dynamics in microresonators. *Nat. Commun.* **8**, 14569 (2017).
63. Lucas, E., Karpov, M., Guo, H., Gorodetsky, M. L. & Kippenberg, T. J. Breathing dissipative solitons in optical microresonators. *Nat. Commun.* **8**, 736 (2017).
64. Wan, S. et al. Frequency stabilization and tuning of breathing solitons in Si₃N₄ microresonators. *Photonics Res.* **8**, 1342–1349 (2020).
65. Bao, C. et al. Observation of breathing dark pulses in normal dispersion optical microresonators. *Phys. Rev. Lett.* **121**, 257401 (2018).
66. Yang, Q. F., Yi, X., Yang, K. Y. & Vahala, K. Stokes solitons in optical microcavities. *Nat. Phys.* **13**, 53–57 (2017).
67. Tan, T. et al. Multispecies and individual gas molecule detection using Stokes solitons in a graphene over-modal microresonator. *Nat. Commun.* **12**, 6716 (2021).
68. Cole, D. C., Lamb, E. S., Del’Haye, P., Diddams, S. A. & Papp, S. B. Soliton crystals in Kerr resonators. *Nat. Photonics* **11**, 671–676 (2017).
69. Yao, B. et al. Gate-tunable frequency combs in graphene-nitride microresonators. *Nature* **558**, 410–414 (2018).
70. Karpov, M. et al. Dynamics of soliton crystals in optical microresonators. *Nat. Phys.* **15**, 1071–1077 (2019).
71. Weng, W. et al. Heteronuclear soliton molecules in optical microresonators. *Nat. Commun.* **11**, 2402 (2020).
72. Bao, H. et al. Laser cavity-soliton microcombs. *Nat. Photonics* **13**, 384–389 (2019).
73. Rowley, M. et al. Self-emergence of robust solitons in a microcavity. *Nature* **608**, 303–309 (2022).
74. Cutrona, A. et al. Stability of laser cavity-solitons for metrological applications. *Appl. Phys. Lett.* **122**, 121104 (2023).
75. Huang, S. W. et al. Mode-locked ultrashort pulse generation from on-chip normal dispersion microresonators. *Phys. Rev. Lett.* **114**, 053901 (2015).
76. Rivas, P. P., Gomila, D., Knobloch, E., Coen, S. & Gelens, L. Origin and stability of dark pulse Kerr combs in normal dispersion resonators. *Opt. Lett.* **41**, 2402–2405 (2016).
77. Xue, X., Wang, P.-H., Xuan, Y., Qi, M. & Weiner, A. M. Microresonator Kerr frequency combs with high conversion efficiency. *Laser Photonics Rev.* **11**, 1600276 (2017).
78. Fulop, A. et al. High-order coherent communications using mode-locked dark-pulse Kerr combs from microresonators. *Nat. Commun.* **9**, 1598 (2018).
79. Chang, L., Liu, S. & Bowers, J. E. Integrated optical frequency comb technologies. *Nat. Photonics* **16**, 95–108 (2022).
80. Bao, C. et al. Nonlinear conversion efficiency in Kerr frequency comb generation. *Opt. Lett.* **39**, 6126–6129 (2014).
81. Jang, J. K. et al. Conversion efficiency of soliton Kerr combs. *Opt. Lett.* **46**, 3657–3660 (2021).
82. Wang, P.-H. et al. Intracavity characterization of micro-comb generation in the single-soliton regime. *Opt. Express* **24**, 10890–10897 (2016).
83. Yi, X., Yang, Q.-F., Yang, K. Y. & Vahala, K. Theory and measurement of the soliton self-frequency shift and efficiency in optical microcavities. *Opt. Lett.* **41**, 3419–3422 (2016).
84. Dmitriev, N. Y. et al. Hybrid integrated dual-microcomb source. *Phys. Rev. Appl.* **18**, 034068 (2022).
85. Lu, Z. et al. Synthesized soliton crystals. *Nat. Commun.* **12**, 3179 (2021).
86. Kim, B. Y. et al. Turn-key, high-efficiency Kerr comb source. *Opt. Lett.* **44**, 4475–4478 (2019).
87. Boggio, J. M. C. et al. Efficient Kerr soliton comb generation in microresonator with interferometric back-coupling. *Nat. Commun.* **13**, 1292 (2022).

88. Godey, C. et al. Stability analysis of the spatiotemporal Lugiato-Lefever model for Kerr optical frequency combs in the anomalous and normal dispersion regimes. *Phys. Rev. A* **89**, 03814 (2014).
89. Mosca, S. et al. Modulation instability induced frequency comb generation in a continuously pumped optical parametric oscillator. *Phys. Rev. Lett.* **121**, 093903 (2018).
90. Weng, H. et al. Dual-mode microresonators as straightforward access to octave-spanning dissipative Kerr solitons. *APL Photonics* **7**, 066103 (2022).
91. Ye, Z., Twayana, K., Andrekson, P. A. & Torres-Company, V. High-Q Si_3N_4 microresonators based on a subtractive processing for Kerr nonlinear optics. *Opt. Express* **27**, 35719–35727 (2019).
92. Zang, J., Yu, S.-P., Carlson, D. R., Briles, T. C., & Papp, S. B. Laser-power consumption of soliton formation in a bidirectional Kerr resonator. arXiv: 2401.16740 [physics.optics].
93. Lugiato, L. A. & Lefever, R. Spatial dissipative structures in passive optical-systems. *Phys. Rev. Lett.* **58**, 2209–2211 (1987).
94. Haelterman, M., Trillo, S. & Wabnitz, S. Dissipative modulation instability in a nonlinear dispersive ring cavity. *Opt. Commun.* **91**, 401–407 (1992).
95. Wabnitz, S. Suppression of interactions in a phase-locked soliton optical memory. *Opt. Lett.* **18**, 601–603 (1993).
96. Gaertner, J. et al. Bandwidth and conversion efficiency analysis of dissipative Kerr soliton frequency combs based on bifurcation theory. *Phys. Rev. A* **100**, 033819 (2019).
97. Kondratiev, N. M., Lobanov, V. E., Cordette, S. J., & Bilenko, I. A. Kerr soliton comb generation efficiency in microresonators and microresonator coupling rate. *Conference on Quantum and Nonlinear Optics IX* **12323** (1232303) (2022).
98. Cui, W. et al. High energy efficiency soliton microcomb generation in high coupling strength, large mode volume, and ultra-high-Q microcavity. *Chin. Opt. Lett.* **21**, 101902 (2023).
99. Leo, F. et al. Temporal cavity solitons in one-dimensional Kerr media as bits in an all-optical buffer. *Nat. Photonics* **4**, 471–476 (2010).
100. Anderson, M. H. et al. Photonic chip-based resonant supercontinuum via pulse-driven Kerr microresonator solitons. *Optica* **8**, 771–779 (2021).
101. Anderson, M. H. et al. Zero dispersion Kerr solitons in optical microresonators. *Nat. Commun.* **13**, 4764 (2022).
102. Xu, Y. et al. Frequency comb generation in a pulse-pumped normal dispersion Kerr mini-resonator. *Opt. Lett.* **46**, 512–515 (2021).
103. Li, Z., Xu, Y., Coen, S., Murdoch, S. G. & Erkintalo, M. Experimental observations of bright dissipative cavity solitons and their collapsed snaking in a Kerr resonator with normal dispersion driving. *Optica* **7**, 1195–1203 (2020).
104. Li, T., Wu, K., Zhang, X., Cai, M. & Chen, J. Experimental observation of stimulated Raman scattering enabled localized structure in a normal dispersion FP resonator. *Optica* **10**, 1389–1397 (2023).
105. Xiao, Z. et al. Modeling the Kerr comb of a pulse pumped F-P microresonator with normal dispersion. *J. Lightwave Technol.* **41**, 7408–7417 (2023).
106. Xu, Y. et al. Harmonic and rational harmonic driving of microresonator soliton frequency combs. *Optica* **7**, 940–946 (2020).
107. Huang, Y. et al. Temporal soliton and optical frequency comb generation in a Brillouin laser cavity. *Optica* **6**, 1491–1497 (2019).
108. Zhang, X. et al. Flat-top soliton frequency comb generation through intra-cavity dispersion engineering in a Brillouin laser cavity. *J. Lightwave Technol.* **41**, 1820–1833 (2023).
109. Jang, J. K., Erkintalo, M., Coen, S. & Murdoch, S. G. Temporal tweezing of light through the trapping and manipulation of temporal cavity solitons. *Nat. Commun.* **6**, 7370 (2015).
110. Hendry, I. et al. Spontaneous symmetry breaking and trapping of temporal Kerr cavity solitons by pulsed or amplitude-modulated driving fields. *Phys. Rev. A* **97**, 053834 (2018).
111. Anderson, M. H. et al. Dissipative solitons and switching waves in dispersion-modulated Kerr cavities. *Phys. Rev. X* **13**, 011040 (2023).
112. Chang, H. C. Stability analysis of self-injection-locked oscillators. *IEEE Trans. Microw. Theory Tech.* **51**, 1989–1993 (2003).
113. Choi, J. J. & Choi, G. W. Experimental observation of frequency locking and noise reduction in a self-injection-locked magnetron. *IEEE Trans. Electron Devices* **54**, 3430–3432 (2007).
114. Liang, W. et al. Ultralow noise miniature external cavity semiconductor laser. *Nat. Commun.* **6**, 7371 (2015).
115. Voloshin, A. S. et al. Dynamics of soliton self-injection locking in optical microresonators. *Nat. Commun.* **12**, 235 (2021).
116. Hu, J. et al. Reconfigurable radiofrequency filters based on versatile soliton microcombs. *Nat. Commun.* **11**, 4377 (2020).
117. Liu, H. et al. Observation of deterministic double dissipative-Kerr-soliton generation with avoided mode crossing. *Phys. Rev. Res.* **5**, 013172 (2023).
118. Wang, W. et al. Robust soliton crystals in a thermally controlled microresonator. *Opt. Lett.* **43**, 2002–2005 (2018).
119. Li, J. et al. Thermal tuning of mode crossing and the perfect soliton crystal in a Si_3N_4 microresonator. *Opt. Express* **30**, 13690–13698 (2022).
120. Yuan, J. et al. Defective soliton crystal microcomb in silicon nitride microresonator. *Asia Communications and Photonics Conference (ACP) / International Conference on Information Photonics and Optical Communications (IPOC)* p 1896–1898 (2022).
121. Afridi, A. A. et al. Versatile octave-spanning soliton crystals with high conversion efficiency in a Si_3N_4 microresonator. *Opt. Express* **31**, 33191–33199 (2023).
122. Fujii, S. & Tanabe, T. Dispersion engineering and measurement of whispering gallery mode microresonator for Kerr frequency comb generation. *Nanophotonics* **9**, 1087–1104 (2020).
123. Lobanov, V. E., Kondratiev, N. M., Shitikov, A. E., Galiev, R. R. & Bilenko, I. A. Generation and dynamics of solitonic pulses due to pump amplitude modulation at normal group-velocity dispersion. *Phys. Rev. A* **100**, 013807 (2019).
124. Liu, H. et al. Stimulated generation of deterministic platicon frequency microcombs. *Photonics Res.* **10**, 1877–1885 (2022).
125. Yu, S.-P., Lucas, E., Zang, J. & Papp, S. B. A continuum of bright and dark-pulse states in a photonic-crystal resonator. *Nat. Commun.* **13**, 3134 (2022).
126. Nazemosadat, E. et al. Switching dynamics of dark-pulse Kerr frequency comb states in optical microresonators. *Phys. Rev. A* **103**, 013513 (2021).
127. Lobanov, V. E., Lihachev, G., Kippenberg, T. J. & Gorodetsky, M. L. Frequency combs and platicons in optical microresonators with normal GVD. *Opt. Express* **23**, 7713–7721 (2015).
128. Lihachev, G. et al. Platicon microcomb generation using laser self-injection locking. *Nat. Commun.* **13**, 1771 (2022).
129. Yu, S.-P. et al. Spontaneous pulse formation in edgeless photonic crystal resonators. *Nat. Photonics* **15**, 461–467 (2021).
130. Li, J. et al. Symmetrically dispersion-engineered microcombs. *Commun. Phys.* **6**, 335 (2023).
131. Xia, D. et al. Integrated chalcogenide photonics for microresonator soliton combs. *Laser Photonics Rev.* **17**, 2200219 (2023).
132. Shu, H. et al. Submilliwatt, widely tunable coherent microcomb generation with feedback-free operation. *Adv. Photonics* **5**, 036007 (2023).
133. Shu, H. et al. Microcomb-driven silicon photonic systems. *Nature* **605**, 457–463 (2022).
134. Peccianti, M. et al. Demonstration of a stable ultrafast laser based on a nonlinear microcavity. *Nat. Commun.* **3**, 765 (2012).
135. Nie, M. et al. Dissipative soliton generation and real-time dynamics in microresonator-filtered fiber lasers. *Light Sci. Appl.* **11**, 296 (2022).

136. Bao, H. et al. Turing patterns in a fiber laser with a nested microresonator: robust and controllable microcomb generation. *Phys. Rev. Res.* **2**, 023395 (2020).
137. Nie, M. et al. Turnkey photonic flywheel in a microresonator-filtered laser. *Nat. Commun.* **15**, 55 (2024).
138. Zhou, L. & Poon, A. W. Electrically reconfigurable silicon microring resonator-based filter with waveguide-coupled feedback. *Opt. Express* **15**, 9194–9204 (2007).
139. Gong, Z. et al. Photonic dissipation control for Kerr soliton generation in strongly Raman-active media. *Phys. Rev. Lett.* **125**, 183901 (2020).
140. Guan, G. et al. Numerical investigation of on-chip multi-gas sensing using a low-repetition-frequency microcavity Kerr comb with backward interference structure. *J. Lightwave Technol.* **41**, 3208–3224 (2023).
141. Helgason, O. B. et al. Dissipative solitons in photonic molecules. *Nat. Photonics* **15**, 305–310 (2021).
142. Miller, S. A. et al. Tunable frequency combs based on dual microring resonators. *Opt. Express* **23**, 21527–21540 (2015).
143. Kim, B. Y. et al. Coherent combining for high-power Kerr combs. *Laser Photonics Rev.* **17**, 2200607 (2023).
144. Skehan, J. C., Helgason, O. B., Schroeder, J., Torres-Company, V. & Andrekson, P. A. Widely tunable narrow linewidth laser source based on photonic molecule microcombs and optical injection locking. *Opt. Express* **30**, 22388–22395 (2022).
145. Helgason, O. B. et al. Surpassing the nonlinear conversion efficiency of soliton microcombs. *Nat. Photonics* **17**, 992–999 (2023).
146. Girardi, M., Helgason, O. B., Ortega, C. H. L., Rebolledo-Salgado, I. & Torres-Company, V. Superefficient microcombs at the wafer level. *arXiv*, (2023). 2309.02280.
147. Rebolledo-Salgado, I. et al. Platicon dynamics in photonic molecules. *Commun. Phys.* **6**, 303 (2023).
148. Tikan, A. et al. Emergent nonlinear phenomena in a driven dissipative photonic dimer. *Nat. Phys.* **17**, 604–610 (2021).
149. Xue, X., Zheng, X. & Zhou, B. Super-efficient temporal solitons in mutually coupled optical cavities. *Nat. Photonics* **13**, 616–622 (2019).
150. Kondratiev, N. M. et al. Recent advances in laser self-injection locking to high-Q microresonators. *Front. Phys.* **18**, 21305 (2023).
151. Lee, S. H. et al. Towards visible soliton microcomb generation. *Nat. Commun.* **8**, 1295 (2017).
152. Wang, H. et al. Dirac solitons in optical microresonators. *Light Sci. Appl.* **9**, 1–15 (2020).
153. Guo, X. et al. Efficient generation of a near-visible frequency comb via Cherenkov-like radiation from a Kerr microcomb. *Phys. Rev. Appl.* **10**, 014012 (2018).
154. Bruch, A. W. et al. Pockels soliton microcomb. *Nat. Photonics* **15**, 21–27 (2021).
155. Lu, J. et al. Two-colour dissipative solitons and breathers in microresonator second-harmonic generation. *Nat. Commun.* **14**, 2798 (2023).
156. Karpov, M., Pfeiffer, M. H. P., Liu, J., Lukashchuk, A. & Kippenberg, T. J. Photonic chip-based soliton frequency combs covering the biological imaging window. *Nat. Commun.* **9**, 1146 (2018).
157. Cutrona, A. et al. High parametric efficiency in laser cavity-soliton microcombs. *Opt. Express* **30**, 39816–39825 (2022).
158. Ji, Q.-X. et al. Engineered zero-dispersion microcombs using CMOS-ready photonics. *Optica* **10**, 279–285 (2023).
159. Ulanov, A. E. et al. Synthetic reflection self-injection-locked microcombs. *Nat. Photonics* **18**, 294–299 (2024).

Acknowledgements

The work was supported in part by the Key Technologies Research and Development Program under Grant No. 2022YFB2802401, the National Natural Science Foundation of China (NSFC) under the Grant No. 62341508, NSFC Excellent Young Scholars Fund (Overseas) and the Optica Foundation Challenge Award, the Postdoctoral Fellowship Program of CPSF under Grant No. GZC20231555, and the China Postdoctoral Science Foundation under Grant No. 2023M742228.

Author contributions

X. Zhang and X. Ji conceived the work. X. Zhang prepared the manuscript. X. Ji and Y. Su supervised the project. All authors reviewed and edited the manuscript.

Competing interests

The authors declare no competing interests.

Additional information

Correspondence and requests for materials should be addressed to Xingchen Ji.

Reprints and permissions information is available at <http://www.nature.com/reprints>

Publisher's note Springer Nature remains neutral with regard to jurisdictional claims in published maps and institutional affiliations.

Open Access This article is licensed under a Creative Commons Attribution 4.0 International License, which permits use, sharing, adaptation, distribution and reproduction in any medium or format, as long as you give appropriate credit to the original author(s) and the source, provide a link to the Creative Commons licence, and indicate if changes were made. The images or other third party material in this article are included in the article's Creative Commons licence, unless indicated otherwise in a credit line to the material. If material is not included in the article's Creative Commons licence and your intended use is not permitted by statutory regulation or exceeds the permitted use, you will need to obtain permission directly from the copyright holder. To view a copy of this licence, visit <http://creativecommons.org/licenses/by/4.0/>.

© The Author(s) 2024